CAAP Final Report

Date of Report: May 11, 2020

Prepared for: *U.S. DOT Pipeline and Hazardous Materials Safety Administration*

Contract Number: DTPH5616HCAP01

Project Title: Fundamental Mechanochemistry-based Detection of Early Stage Corrosion Degradation of Pipeline Steels

Prepared by: Iowa State University

Contact Information: Professor Ashraf Bastawros,
                       T.A.Wilson Professor of Engineering
                       Department of Aerospace Engineering
                       2271 Howe Hall, Rm 1200
                       Ames, IA 50011-2271
                       Phone: 515-294-3039   Fax: 515-294-3262
                       Email: bastaw@iastate.edu

Fundamental Mechanochemistry-based Detection of Early Stage Corrosion Degradation of Pipeline Steels

Table of Contents

Table of Figures

results for the critical dislocation nucleation load (normalized by that of perfect crystal) as a function of the concentration. The error bar is derived from six different geometric rendering of the model.

Figure 6.4: Atomistic simulation results of perfect crystal showing multiple dislocation nucleation and propagation at the critical loading level. Snapshots of atomistic projection with shading of out-of-registry atoms for the perfect crystal (a-c), hydrogen (d-f), and vacancy cases (g-i), highlighting variation of dislocation nucleation characteristics with addition of lattice vacancies and H interstitials.

Figure 6.5: Distribution of first strain invariant on {001} plane, showing initially induced hydrostatic strain by (a) vacancy and (b) hydrogen atom. (c) The line distribution of first strain invariant along <110> direction (dashed lines on (a) and (b)) presented as a function of distance normalized by the atomic distance.

1. Introduction

Stress Corrosion Cracking (SCC) on the external surface of a pipeline is one of the primary degradation modes in oil and gas pipelines, despite the fundamental understanding of the mechanisms. SCC is characterized by crack growth during corrosion of alloys in the presence of external tensile stress, at a significantly smaller stress compared to unexposed crack growth of the same material system [1-3]. During SCC, the majority of the life of a pipeline remains within the nucleation stage as depicted on Fig. 1.1, wherein micro-damage is percolating very slowly within the prolonged incubation stage [4], and below detection thresholds for commonly deployable nondestructive evaluation techniques. The failure to monitor the changes in parameters germane to corrosion poses an especially severe safety threat [5, 6], and will be an increasing concern due to aging infrastructure and expense of new construction.
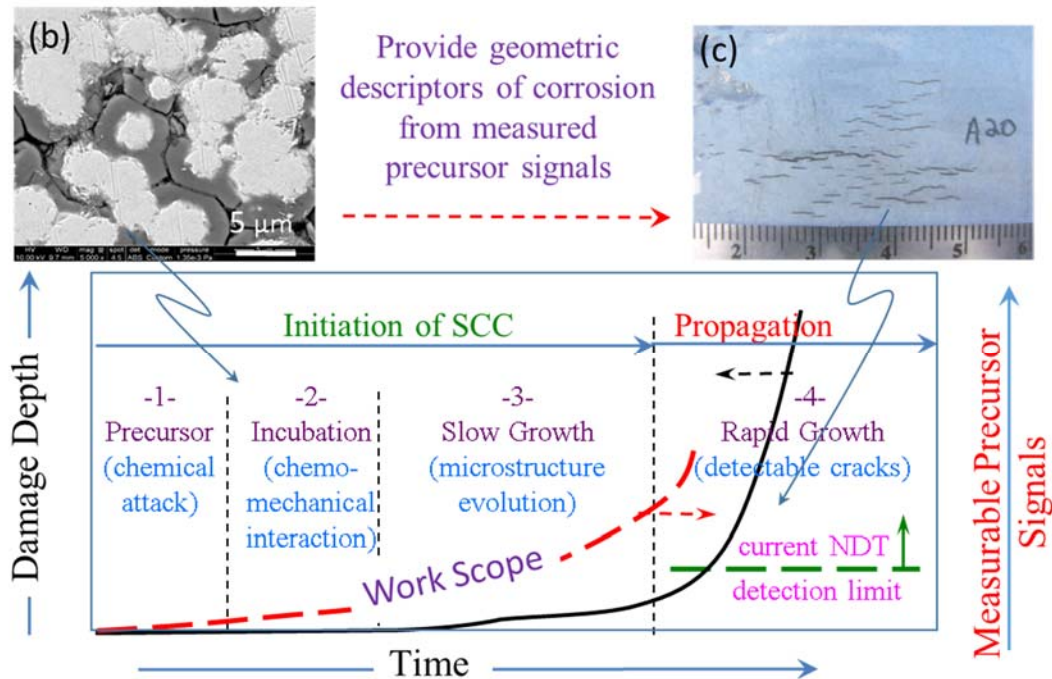
Fig. 1: Scope of the proposed work to quantify measurable precursor signals during SCC initiation (after Staehle, 2010) [4]. (b) Early damage percolation (current CAAP work; micron-range near surface damage). (c) Colonies of SCC (detectable macro-cracks) [6].

The aim of the proposed work is to provide measurable precursor signals associated with the initiation stage of near surface damage and cracking, as depicted on Fig. 1.1. We have identified many salient features during the early stage of the SCC process (Stages 1, 2 on Fig. 1.1), including residual stress build up, near surface (within few microns) defect percolation and changes of dislocation dynamics, and measureable changes of the surface ohmic resistance. We developed model based prediction of the onset and progression of SCC subsurface damage, and assessed the electrochemical impedance spectroscopy (EIS) to measure the extent of surface damage. Such framework would enable the development of appropriate field deployable NDE technology with the needed spatial and temporal resolutions. The proposed framework have the potential to

enhance abilities to better predict remaining safe life, operating pressures and identify the need for mitigation measures to be taken.

2. Background

SCC refers to the failure by cracking of normally ductile metals in corrosive environments, when they are subject to tensile stress. SCC affects a wide range of high strength alloys. For example, 21% of steel pipeline failures are attributable to SCC.[1] Typically, SCC initiates at the protective coating disbondments on the outer surfaces of buried pipelines, at a localized corrosion sites such as pits and grain boundaries. Local soil pH level affects the nature of the cracking as intergranular (ICSCC) for high pH-level (pH >9) and transgarnular (TGSCC) for near neutral pH [7, 8]. The pipeline failure will result in rupture for low aspect ratio cracks (long and shallow) or leakage for high aspect ratio cracks (short and deep) [6]. There is widespread debate about SCC mechanisms, including the contributions of mechanical vs. chemical processes in the initial damage percolation, leading to a macroscopic crack growth and the associated role of hydrogen embrittlement. Several mechanisms suggest that brittle cracking is produced by localized plastic deformation activities caused by dislocation emission and motion accompanying localized corrosion at crack tip [9-11]. Quantification of the progression of these local changes might improve corrosion management through prospective new NDE techniques for early detection of SCC.

Mechanisms proposed for corrosion-induced embrittlement have included formation of geometric features such as notches that concentrate external stress, or creation of brittle surface layers or films on corroding surfaces [16]. Much of the prior research on intergranular corrosion of pipeline steels has concerned on the nature of electrochemical corrosion reactions and products within the critical potential range [17-23]. It is found that dissolution near the potential of the active dissolution current peak produces Fe(II) hydroxide and carbonate species, while at potentials above the active region insoluble Fe(III) products are found. Also, the potential ranges of both IGC and intergranular SCC has been shown to lie between the active peak and the passivation potential, in which both Fe(II) and Fe(III) products are formed. However, this work did not establish a relationship between the electrochemistry of corrosion within the critical potential range and the SCC mechanism. Also, no prior work to our knowledge focused on the role of grain boundaries in the corrosion process, which is clearly central to an understanding of intergranular SCC.

Because of the close coupling between intergranular corrosion and stress corrosion cracking of pipeline steels, it is important to identify aspects of corrosion at grain boundaries that are relevant to the evolving mechanical properties of the near-surface region. Corrosion morphology development is potentially significant because the geometry of the corroded region determines its response to external tensile stress. Further, intergranular corrosion rates can be inferred by observing grain boundary morphology evolution. Despite the relevance of intergranular corrosion to high-pH SCC of pipeline steels, no detailed characterization of grain boundary morphology evolution during IGC of ferritic steels has been reported in the literature, in contrast to the knowledge base about such processes on austenitic stainless steels [24]. Also, it has been proposed

that corrosion-induced wedging stress at grain boundaries can assist crack initiation and growth [25-28]. However, very few studies exist on stress evolution accompanying corrosion along grain boundaries.

3. Objective of the Proposed Work:

The proposed research plan focuses on model-aided development of experimental protocols that provide measureable precursor signals, which correlate to geometrical descriptors of the subsurface damage. The focus is on measurable degradation parameters that can assist in the development of NDE measurement procedures. The project objective is to assess the feasibility of detection and monitoring of initial subsurface damage to shallow crack formation, with focus on:

(1) ***Develop the mechanochemistry modeling framework for early stage SCC:*** Understand the synergistic role of mechanical loading and chemical kinetics to predict the onset and evolution of corrosion as well as spatial residual stress development, and prospectively increase the pipeline total fatigue life.

(2) ***Quantify the physical and mechanical changes during the early stage of SCC by EIS:*** Arriving at measureable physical and mechanical quantities and their correlation to the geometrical descriptors of corrosion and/or SCC will provide the pathway for development of corrosion mitigation strategies, as well as in-line inspection (ILI) methodologies.

(3) ***Assist the future development of multi-scale multi-physics models***: Provide phenomenological understanding, basic modeling framework and laboratory measurements for the degradation process and mechanisms in high strength pipeline steels for enhanced modeling tools to better predict remaining safe life, operating pressures and identify the needed mitigation measures to be taken.

4. Experimental Framework:

Samples of a high strength low-alloy pipeline steel (API X70) were machined from a pipe wall. The specimens of 1 mm thickness were cut along the long axis of the pipe, with the top surface in the longitudinal-short transverse plane. The sample length and width dimensions were 18 mm x 18 mm. The main alloying elements in X70 were Mn (~1.75 wt. %), Si (~0.45 wt. %), and C (~ 0.17 wt. %). The minority pearlite phase was composed of grains less than 5 μm in width and elongated in the longitudinal direction, while the majority ferrite phase was made up of nearly equiaxed grains of typically 5 μm size. The microstructure of X-70 pipeline steel showing strong texture along the rolling direction of the pipe is shown in Fig. 4.1. The sample surfaces were polished with 400, 600 and 800-grit sandpaper, followed by cleaning with deionized water and ethanol. Electrochemical experiments were carried out in a three-electrode cell with Pt wire counter electrode and Ag/AgCl reference electrode, shown in Fig. 4.2. All cited potentials are with respect to this reference. The test solution was naturally aerated aqueous 1 M NaHCO$_3$ at room temperature. Solutions were prepared using analytical grade reagents and deionized water (resistivity 18 MΩ-cm). The applied potential was first held at -1.0 V for 5 min to cathodically

reduce surface oxide, and then stepped or scanned in the anodic direction. For examination of the corrosion morphology in cross section, samples were polished to reveal planes at orientations either perpendicular to or at a shallow angle from the surface. In addition, focused ion beam (FIB) microscopy cross sections were prepared by etching at 52° from the surface (FEI NanoLab Helios Dual Beam). Corrosion specimens were examined by scanning electron microscopy (SEM, FEI Quanta 250), and by non-contact optical profilometry (Zygo NewView 6200).
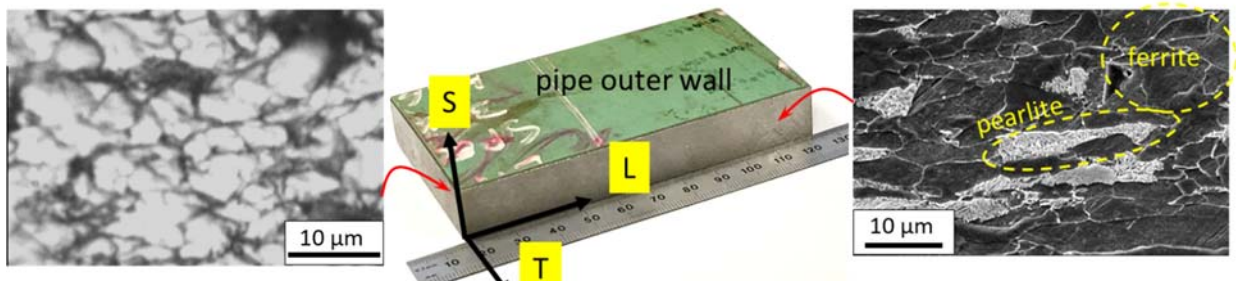
Fig. 4.1: Microstructure of X-70 pipeline steel showing strong texture along the rolling direction of the pipe.
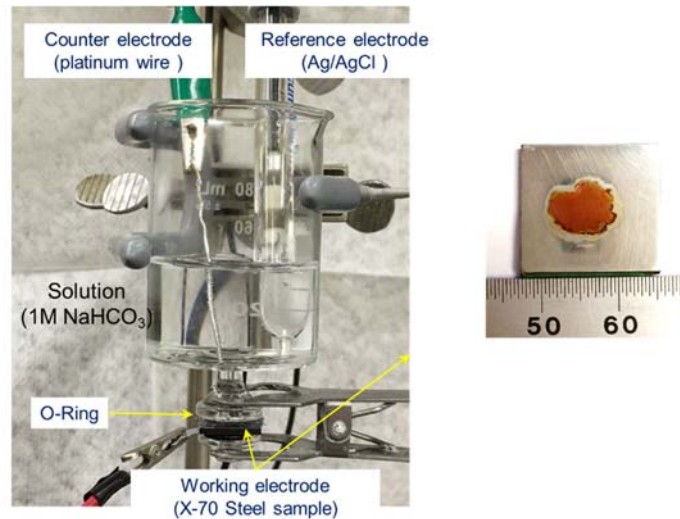
Fig. 4.2: The utilized electrochemical cell showing the conventional three electrode, with steel samples as working electrode, platinum wire as counter electrode and Ag/AgCl reference electrode. Gamry Reference 3000 potentiostat was used as the power source. Dow Corning Vacuum Lubricant was applied between the sample and the O-ring to eliminate crevice corrosion.

In situ stress measurements employed the phase shifting curvature interferometry method [31]. The applications of this technique to measure stress changes during corrosion and anodic oxidation of aluminum were described in earlier publications [28, 32]. The utilized interfermetric setup is shown in Fig. 4.3 One side of the steel sample was polished to a 0.05 μm particle finish using a diamond particle suspension and served as a reflective surface for interferometry. The specimen was mounted in a test cell with the unpolished side in contact with the electrolyte solution and the

opposite side facing the optical system. Changes in sample curvature during corrosion were monitored. The curvature change ($d\kappa$) is related to the near-surface force per width (dF_w) according to the Stoney thin-film approximation,

$$dF_w = \frac{Y_s h_s^2}{6(1-v_s)} d\kappa \tag{1}$$

where Y_s, v_s and h_s and are respectively the elastic modulus, Poisson's ratio and thickness of the steel sample. The force per width is the in-plane biaxial stress σ_{xx} integrated through the sample thickness,

$$F_w = \int_0^{h_s} \sigma_{xx} dz \tag{2}$$

where the x axis is parallel to the steel surface, and the z axis extends toward the bulk metal from its origin at the surface. Force per width is referenced to the initial state of the sample at the beginning of anodic polarization. Compressive and tensile force changes are respectively negative and positive in sign.
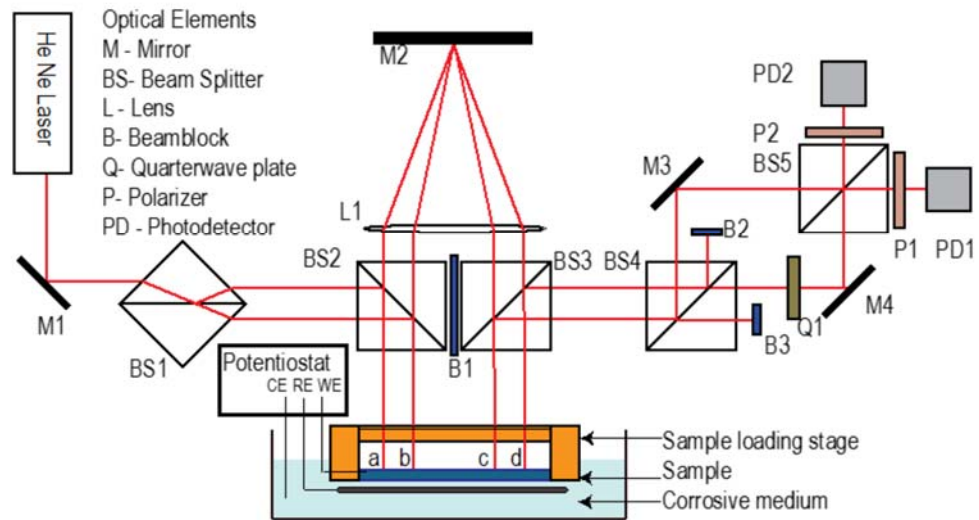
Fig. 4.3: Schematic of the setup of interferometry system, which also shows the setup of the samples.

5. Results on Morphology and Stress Evolution During the Initial Stages of Intergranular Corrosion of X70 Steel

5.1 Electrochemical measurements

Figure 5.1 (a) shows the active dissolution region of the polarization curve of X70 steel in 1 M NaHCO$_3$ solution. The potential region of susceptibility to IGC and SCC extends from the potential of the current peak at -0.6 V to the passivation potential at -0.4 V [12,14,15]. Three test potentials within this range were selected for potentiostatic experiments, as indicated in the Figure: -0.575 V, -0.521 V and -0.478 V. Examples of current transients at these potentials are shown in Fig. 5.1 (b). Initially, the current density decayed to a minimum value at 1 - 6 min at all three potentials. From rotating ring-disk electrode (RRDE) experiments Riley and Sykes found that the main reaction during the current decay is formation of a surface film [21]. Based on the charge density of 10 to 30 mC/cm^2 passed during the decay, the equivalent Fe(OH)$_2$ thickness is 14 - 40 nm, comparable to the thickness of 80 nm from XPS for the steady-state surface film at the peak potential [14]. At the two higher potentials, the current increased to a maximum after the initial decay and then slowly fell. No maximum was reached after 45 min at -0.575 V.
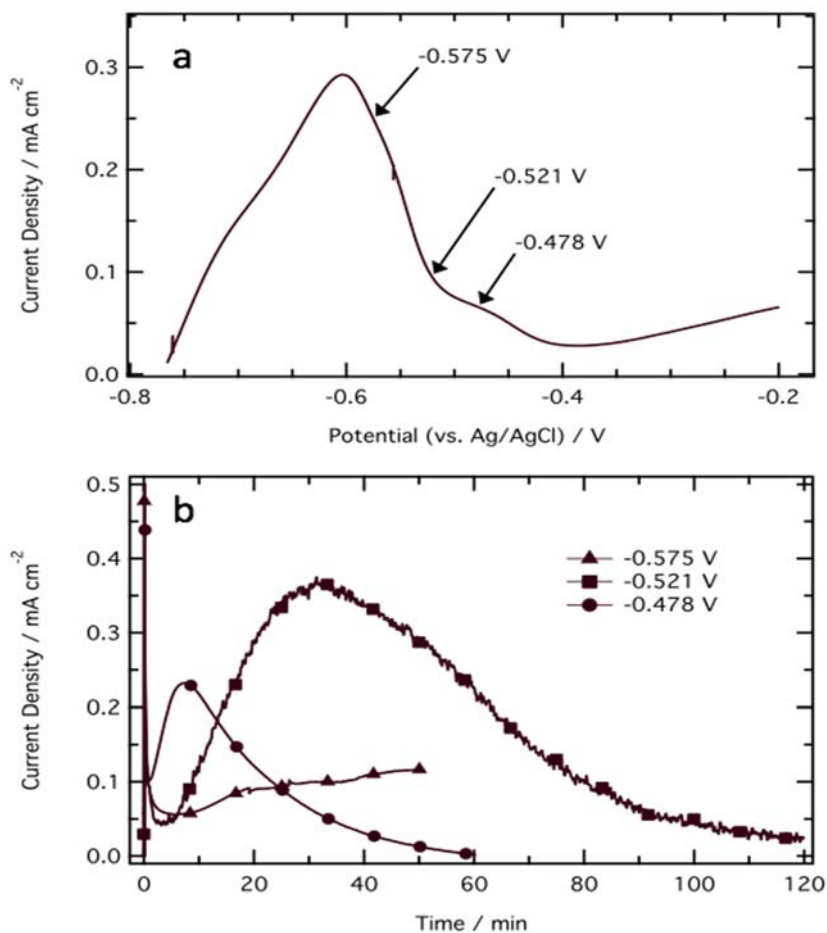
Fig. 5.1: Electrochemical measurements during corrosion of X70 steel in 1 M NaHCO$_3$. (a) Linear sweep voltammetry showing the three test potentials used in other experiments. (b) Current density transients for the experiments used for morphology observations in Figs. 4-7.

11

5.2. Large-angle cross-section samples

Large-angle cross section views of the steel interface after corrosion tests at -0.521 V for 2 and 4 hr are exhibited in Fig. 5.2 (a) and 2 (b) respectively. The 2 hr-exposed sample was prepared by FIB milling and the 4 hr sample by cross-sectioning and mechanical polishing. The along the top surface Both images illustrate the corrosion product film that covered the steel surface after the current density maximum. The white-shaded material is the steel and the dark gray-shaded layer on its upper surface is corrosion product. The corrosion product consists of particles several μm in width separated by small gaps. The void in the central part of the film in Fig. 5.2 (a) is atypical and may be caused by attrition of a corrosion product particle during sample preparation. EDS of the corrosion product layer in Fig. 5.2 (b) revealed that it contained Fe, O and C, suggesting that the film is an iron hydroxy-carbonate as found previously [18, 22, 23]. The Na/Fe concentration ratio of 0.15 indicated that the product contained significant amount of sodium, consistent with the finding of sodium or potassium in the corrosion product in earlier studies [18, 23]. Incorporation of electrolyte Na^+ ions is evidence that the product is formed by precipitation. Nanoindentation measurements revealed an elastic modulus of 28 GPa for the product layer, much smaller than the value of about 200 GPa for dense iron oxide [30, 33]. The low modulus of the film suggests high porosity, also consistent with a precipitated film.
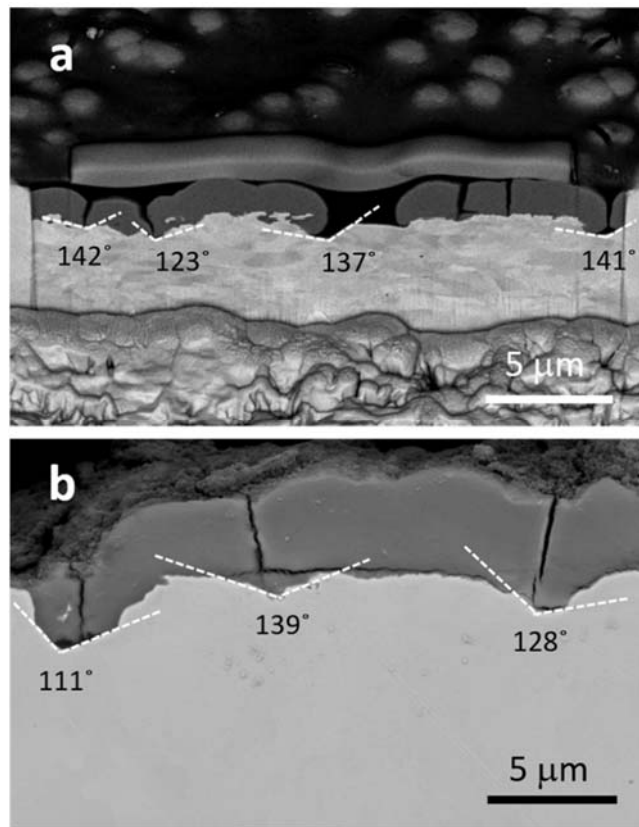
Fig. 5.2: Large-angle cross section views after corrosion at -0.521 V. (a) 2 hr exposure; sample prepared by FIB etching, cross section plane 45° from horizontal. (b) 4 hr exposure; sample prepared by polishing, cross section plan 90° from horizontal. Dashed lines indicate triangular wedge features produced by corrosion at the alloy-corrosion product interface. The angles of the wedge apex are marked in the image.

The precipitated corrosion product layer thickness measured from the cross-section images increased from 2.5 μm at 2 hr to 4.3 μm at 4 hr. The corresponding ratios of thickness to charge density were 1.9 x 10^{-4} cm^3/C at 2 hr and 1.6 x 10^{-4} cm^3/C at 4 hr. These values can be compared to the ratios associated with possible product layer constituents. The corrosion product formed in bicarbonate solutions is an iron hydroxycarbonate [23], which at -0.521 V may contain both and Fe(II) and Fe(III) compounds [17, 18, 21, 22]. The thickness-charge density ratio for compact product layers based on the molar volumes of $Fe(OH)_2$, $FeCO_3$ and $Fe(OH)_3$ are respectively 1.4 x 10^{-4} , 1.5 x 10^{-4} and 9.5 x 10^{-5} cm^3/C. The porosity of the product layer is consistent with the somewhat larger ratios found experimentally.

The images in Fig. 5.2 (a) and (b) reveal a number of triangular wedges along the metal-corrosion product interface, marked by dashed lines. The wedges are positioned close to the gaps between corrosion product particles. These features were especially evident during FIB examination for Fig. 5.2 (a), as numerous wedge features located at different points on the surface appeared and disappeared as the sample cross section was ion-milled. The wedge angle is defined as shown in Fig. 5.2 as the angle at the apex of the triangular groove. Based on about 8 measurements at each exposure time, the wedge angle was $136 \pm 6.4°$ at 2 hr and $117 \pm 17°$ at 4 hr. The wedge depths are about 0.6 μm at 2 hr and 1 to 1.5 μm at 4 hr. Triangular wedges can be produced by intergranular attack, as discussed in the next section.
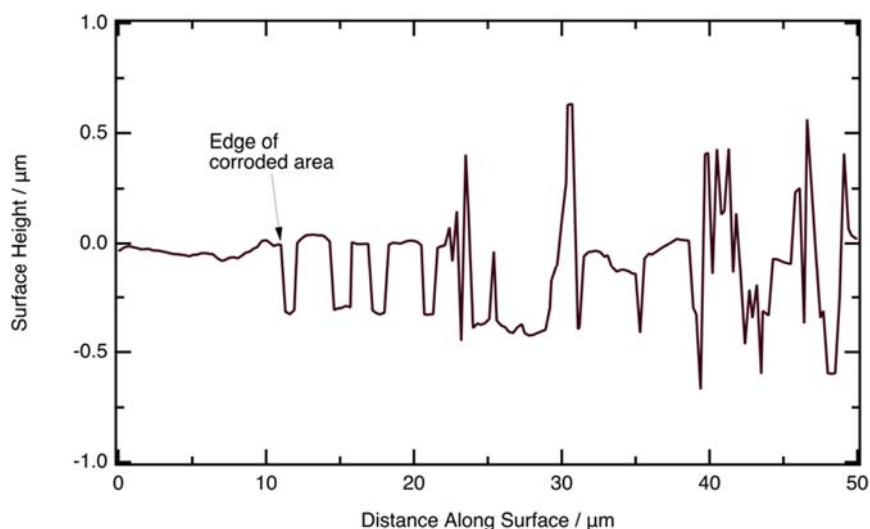
Fig. 5.3: Height profile measured by optical profilometry after 2 hr exposure at -0.521 V and followed by removal of corrosion product. Curve to the left of the arrow represents an area that was not exposed to solution.

Figure 5.3 exhibits a non-contact optical topological scan for an experiment in which the sample was exposed for 2 hr at -0.521 V. After the experiment, the corrosion product was removed by wiping the surface with a swab dipped in acetic acid. The profile spans parts of the rough corroded surface as well as surrounding surface (abscissa values smaller than 10 μm) that was not exposed to solution. The corroded area reveals minima with depths from 0.3 to 0.7 μm below the uncorroded area, and peaks that rise above the surrounding

surface. The minima are apparently the triangular wedges marked by dashed lines in Fig. 5.2 (a), as both features have the same range of depths and similar lateral spacing. The peaks are likely remnants of corrosion product particles. If these particles are disregarded, the top surface heights inside and outside the corroded area are the same. It can therefore be concluded that there was no significant general corrosion on the surface between the triangular wedges. A similar profile measured after 4 hr (not shown) also supports the absence of general corrosion. Thus, despite the overall appearance of the product layer as a uniform film, the corrosion process seems to exclusively consist of localized attack centered at shallow triangular wedges.
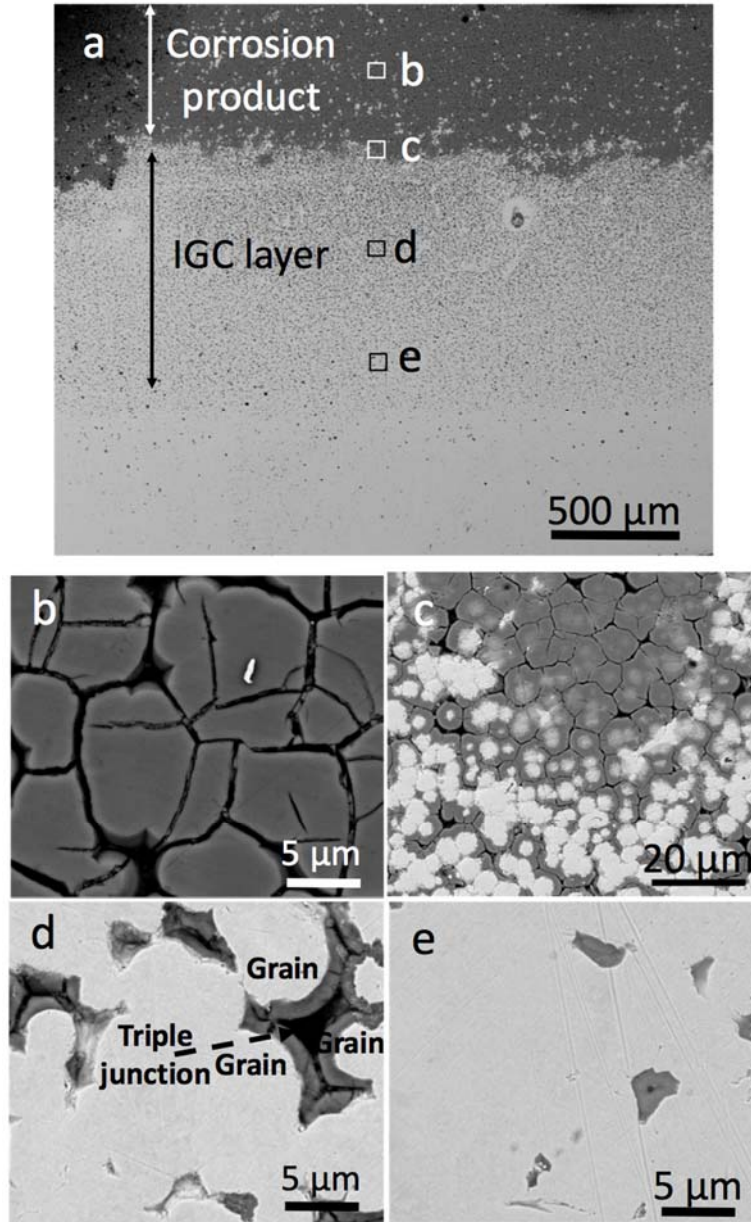
Fig. 5.4: Small-angle cross section views of X70 steel after 2 hr corrosion at -0.521 V. Sample was prepared by shallow-angle polishing. Panels (b) - (e) are high-magnification images at the points indicated in the low-magnification image (a).

5.3. Small-angle cross section samples

Small-angle cross sections were prepared by polishing to reveal the internal corrosion morphology on planes nearly parallel to the external surface. Figure 5.4 exhibits SEM images of a steel specimen after a 2 hr corrosion exposure at -0.521 V. The current density transient for the same experiment is found in Fig. 5.1 (b). In the low magnification image in Fig. 5.4 (a), the intergranular corrosion layer lies between the precipitated corrosion product and uncorroded base alloy. The layer labeled corrosion product in Fig. 5.4 (a) is the same as the precipitated iron hydroxide-carbonate layer noted in Fig. 5.2. Note that distances along the vertical direction in these images magnify depth through the polishing angle. The magnification factor in this direction is approximately 1000, since the apparent thickness of the IGC layer in Fig. 5.4 (a) is 900 μm, while the FIB cross section (Fig. 5.2 (a)) reveals the true IGC layer thickness to be 0.9 μm. Figs. 5.4 (b) - (e) are higher-magnification views at selected depths within the IGC layer. Figs. 4 (d) and (e) illustrate that localized corrosion attack centers at grain boundary triple junctions between the equiaxed and approximately 5 μm diameter steel grains. Black-shaded crevices formed by corrosion at triple junctions are surrounded by roughly 1 μm thick gray-shaded corrosion product layers coating the white-shaded steel grains. In addition to progressing along the triple junctions, corrosion also penetrates laterally along the grain boundaries adjacent to the triple junctions (Fig 5.4 (d)). At the interface between the metal and the top corrosion product layer (Fig. 5.4 (c)), the grain boundary product film surrounds isolated clusters of grains. The cores of these grain clusters are eventually converted to corrosion product, forming the particles comprising the film. Thus, the corrosion product morphology reflects that of the underlying grain structure.

The crevices along triple junctions in Fig. 5.4 correspond to the fissures at the triangular wedges in Fig. 5.2. Therefore, Figs. 5.4 (c) - (e) represent respectively the top, midpoint and apex of the triangular wedges in Fig. 5.2. Note that triple junction crevices are present in Fig. 5.2 only when the cross section plane lies close to the wedge apex. Since the triangular wedges are centered at triple junctions, they are indeed associated with intergranular attack. Triangular wedges have been observed during intergranular corrosion of austenitic stainless steels at transpassive potentials, and are considered to be characteristic features of "unsensitized" IGC in the absence of grain boundary precipitates [16, 26]. The wedge angle α is related to the ratio of the dissolution velocity of the grain boundary at the wedge apex (V_{gb}) to the wedge surface dissolution velocity (V_s),

$$\frac{V_{gb}}{V_s} = \frac{1}{sin(\alpha/2)} \tag{3}$$

The wedge angles in the present work suggest V_{gb}/V_s of 1.1 - 1.2, much smaller than the ratio of approximately 10 indicated by the relatively acute wedge angles in stainless steel [16]. To our knowledge, the triangular wedge morphology of IGC in pipeline steel has not been previously noted. However, Wendler-Kalsch found that corrosion in the potential range of SCC susceptibility produced 2 μm-deep grain boundary grooves similar in appearance to the wedges in Fig. 5.2 [5]. No such grooves were observed in Ref. [5] at potentials higher than the upper limit of the SCC potential range, suggesting that the fundamental processes that produce the grain boundary wedge shape may intrinsically important in the SCC mechanism.

The important features of the intergranular corrosion geometry are depicted schematically in Fig. 5.5, which shows the triangular wedge morphology at the corroded triple junction. The wedge

angle α and the corrosion velocities V_s and V_{gb} are defined. Fig. 5.5 also illustrates the precipitated porous corrosion product layer in Figs. 5.2 and 5.4 (a), and an underlying compact layer between the precipitate and the steel. Evidence for such a nonporous corrosion product was obtained by nanoindentation measurements, which revealed submicron-thick regions close to the metal with elastic modulus approaching that of compact iron oxide [29, 30].
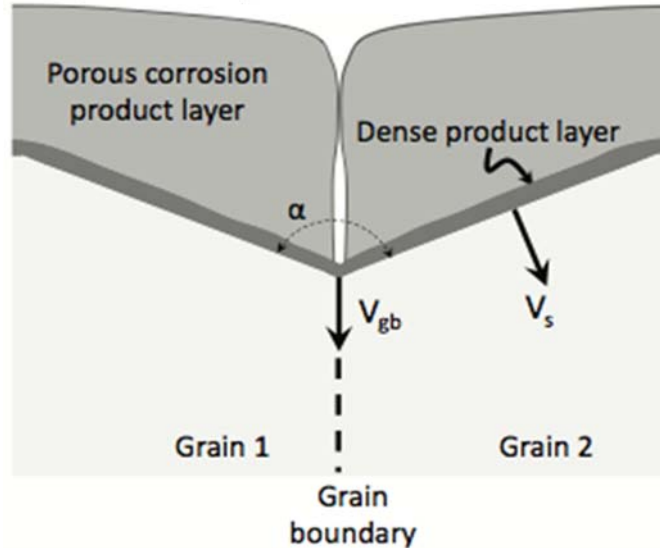
Fig. 5.5: Schematic depiction of triangular wedge morphology of intergranular corrosion.

Figure 5.6 shows an EDS line scan across a corroded grain boundary in a sample exposed for 2 hr at -0.521 V. The major species in the corrosion product layer are iron, oxygen and carbon, consistent with a product layer composed of iron hydroxy-carbonates [23]. The composition is close to that of the top surface corrosion product but without significant levels of sodium deriving from $NaHCO_3$ electrolyte. According to Blengino et al., product layers exhibit variable quantities of incorporated electrolyte ions depending on the corrosion rate [23]. Manganese, the primary alloying element in X70 steel, is apparently selectively excluded from the product layer, while silicon from the alloy is selectively oxidized and incorporated into the product. Silicon can significantly affect IGC in austenitic stainless steels, but we know of no prior reports of silicon effects on IGC or SCC of pipeline steels, or evidence for selective oxidation of Si at grain boundaries in X70 [24, 35]. Prior analytical TEM measurements of X52 and X65 steels revealed grain boundary segregation of only Mn solute, and atom probe tomography showed evidence for C segregation in X52 and X70 steels [36-38].

Additional small-angle cross sections were prepared on a sample exposed at -0.521 V for 15 min. At these early times, the cross sections revealed scattered corrosion product particles and isolated evidence of grain boundary attack at triple junctions, consistent with previous observations [21, 23]. Therefore, the current rise during polarization at constant potential (Fig. 5.1 (b)) correlates with spreading of intergranular attack to an increasing fraction of the surface grain boundaries. This interpretation was suggested previously by Riley and Sykes [21]. Similar current transients with maxima were recently found during CO_2 corrosion of carbon steel near pH 6, and the current rise was interpreted differently in terms of voids caused by crystallite nucleation in an amorphous surface film, or pH decrease due to carbonate precipitation [39, 40].
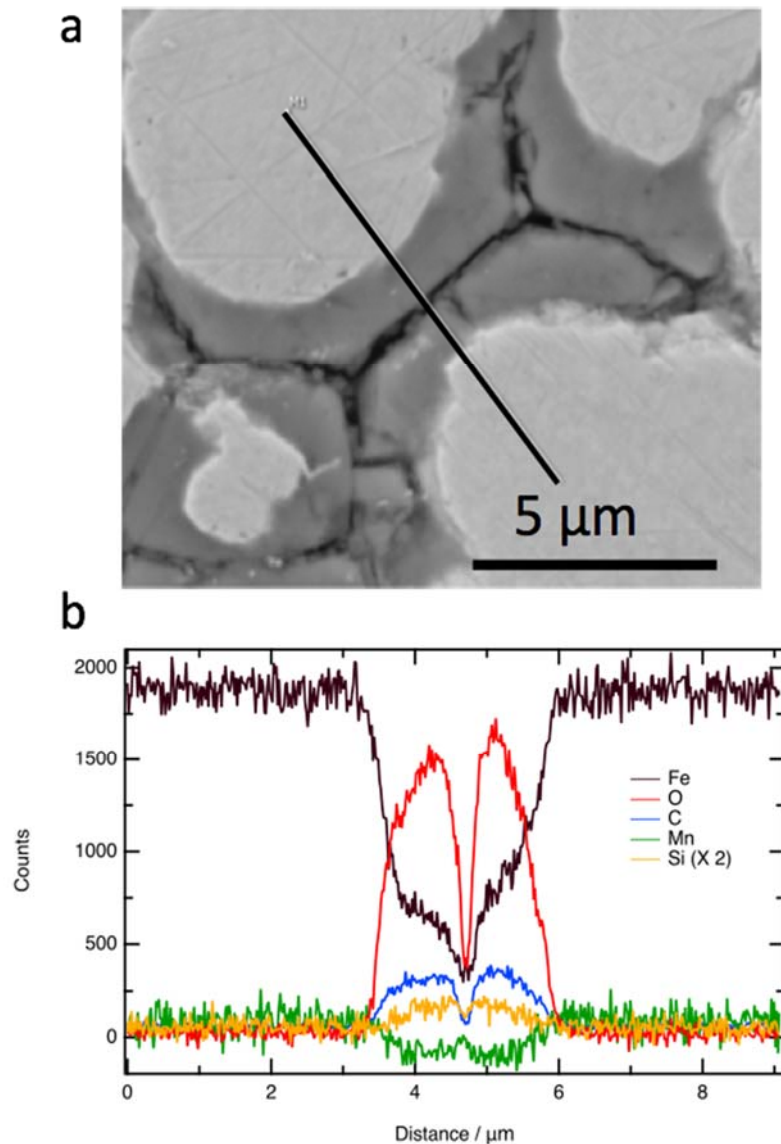
Fig. 5.6: Composition of grain boundary corrosion product film on sample exposed for 2 hr at -0.521 V. (a) SEM showing location of EDS line scan. (b) Composition profile along the line scan.

Figure 5.7 exhibits small-angle cross sections of steel exposed at -0.478 V for 1 hr, for which the current density transient is given in Fig. 5.1 (b). Fig. 5.7 (a) shows the entire thickness of the IGC layer, while Fig. 5.7 (b) represents the interface between steel and the top product layer, and Fig. 5.7 (c) shows the midsection of the corroded region. As at -0.521 V, corrosion at -0.478 V is localized at triple junctions, and extends into lateral grain boundaries surrounding the triple junctions. Comparison of the interface images Fig. 5.7 (b) and Fig. 5.4 (c) reveals that, despite the smaller exposure time at -0.478 V, there is a significantly larger number density of corroded grain boundary triple junctions at the higher potential, and consequently greater penetration of corrosion product between grains. Apparently, the rate of spreading of IGC among grain boundaries increases with potential, correlating with the faster increase of current density with time after the initial minimum (Fig. 5.1 (b)).
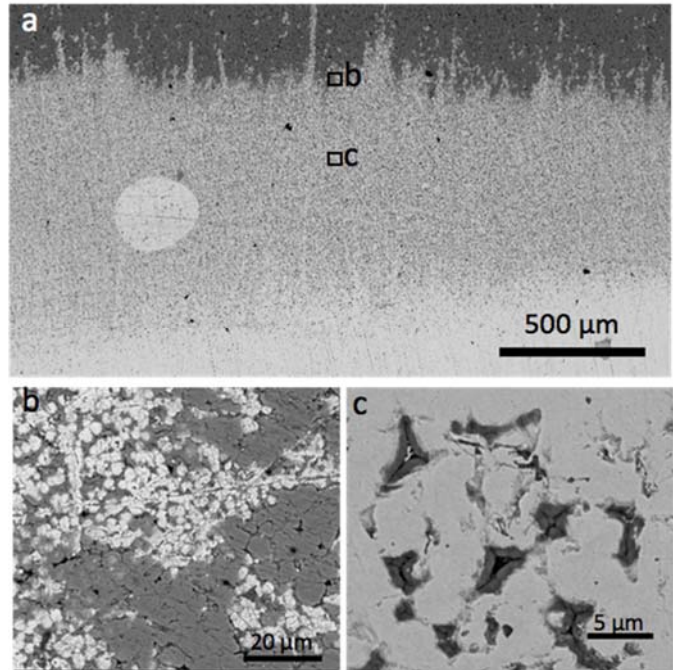
Fig. 5.7: Small-angle cross section views of X70 steel after 1 hr corrosion at -0.478 V. Sample was prepared by shallow-angle polishing. Panels (b) and (c) are high-magnification images at the points indicated in the low-magnification image (a).
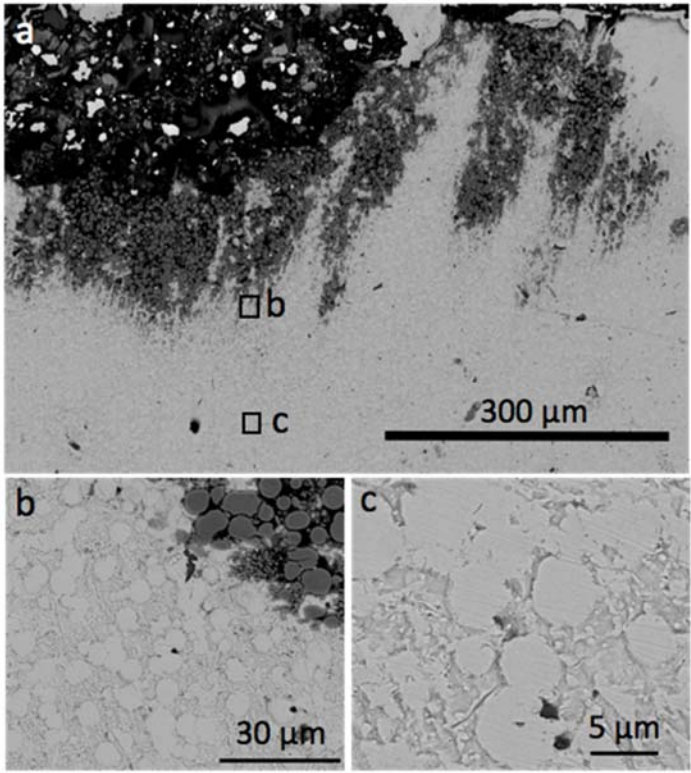
Fig. 5.8: Small-angle cross section views of X70 steel after 50 min corrosion at -0.575 V. Sample was prepared by shallow-angle polishing. Panels (b) and (c) are high-magnification images at the points indicated in the low-magnification image (a).

Figure 5.8 shows small-angle cross sections for a 50 min corrosion experiment at a potential of -0.575 V, close to the active dissolution peak of the steel polarization curve. The susceptibility of steel to SCC is considered to be lower at such potentials in comparison to potentials closer to the passivation potential [12]. The images in Fig. 5.8 represent an area near a deposit of corrosion product, which in this experiment covered only a small portion of the surface. Fig. 5.8 (a) shows the entire thickness of the IGC layer, Fig. 5.8 (b) the steel-product layer interface, and Fig. 5.8 (c) shows the midsection of the corroded region. In contrast to the two more positive potentials, the cross-sectional images at -0.575 V revealed almost no detectable internal corrosion product at grain boundaries. Instead, IGC is characterized by selective dissolution of grains.

5.4. Transient electrochemical and stress measurements

In this section, in situ stress measurements during intergranular corrosion are presented and discussed in view of the observations of IGC morphology evolution. Fig. 5.9 (a) displays current density and force per width transients from experiments at each of the three test potentials, and the charge density obtained by integration of the current is shown in Fig. 5.9 (b). Force per width at -0.478 V and -0.521 V increased steadily in the compressive direction during polarization. After an initial compressive period at -0.575 V, the force changed direction at 9 min, and exhibited a net tensile change at 60 min. From the trends in Fig. 5.9, it is clear that compressive stress generation correlates with internal corrosion product formation: extensive grain boundary corrosion product was found at the two higher potentials, but none at -0.575 V.
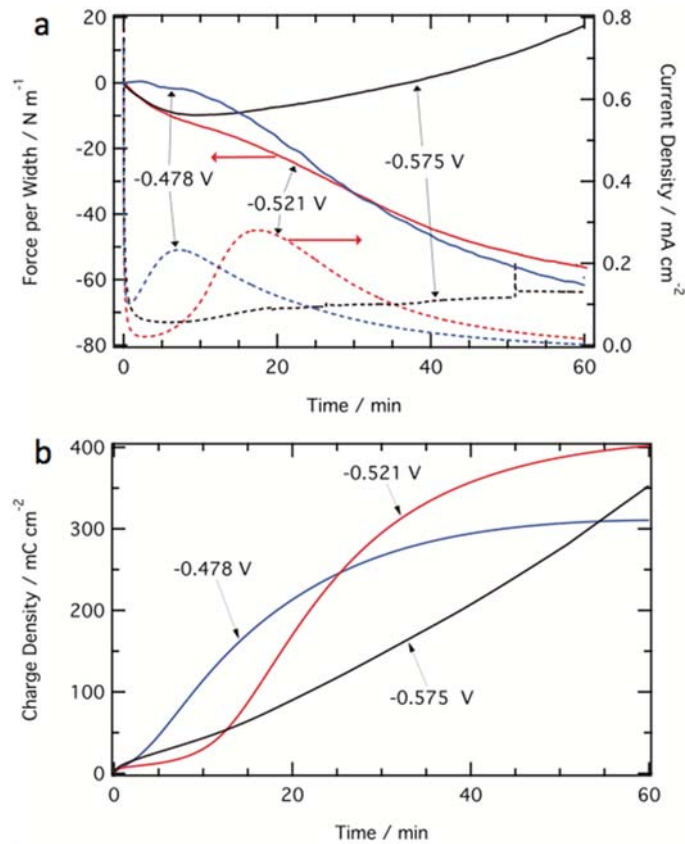
Fig.5.9: Stress and current density measurements during corrosion exposures at the three test potentials. (a) Force per width (solid lines) and current density (dashed lines) transients. (b) Charge density transients obtained by integrating the current density in (a).

Stress is produced during oxide layer formation by strain associated with the volume increase upon conversion of metal to oxide [41]. The same principle can be applied to the present hydroxide-carbonate layers. As a first approximation, stress is modeled in a flat nonporous corrosion product film of uniform thickness, which comprises an inner dense layer between the metal and an outer stress-free porous precipitated corrosion product (Fig. 5.5). As mentioned above, the presence of this compact layer was revealed by nanoindentation measurements [29, 30]. Since adherence of the surface film with the metal requires compatibility of the net in-plane strain at the metal-film interface, the formation of the compact layer must result in elastic or plastic strain within the film. It is assumed that the oxidation-induced strain-thickness product of the film is isotropic and hence given by $\Delta V_{m/f}/3$, where $\Delta V_{m/f}$ is the net volume expansion per unit area at the metal-film interface during metal oxidation [41],

$$\Delta V_{m/f} = \frac{q\Omega_p}{2F}\left(t_A - \frac{1}{\Phi}\right) \tag{4}$$

Here q is the anodic charge density, F is Faraday's constant, Ω_p is the molar volume of corrosion product, Φ is the Pilling-Bedworth ratio (the ratio of corrosion product to metal volume), and t_A is the average transport number for inward electrical migration of OH^- and CO_3^{-2} anions in the product layer. The anion transport number represents the fraction of current associated with film growth at the metal interface, with the remaining fraction $(1 - t_A)$ due to outward metal ion migration resulting in growth of the precipitated film. In Eq. (11), t_A is the thickness of corrosion product formed at the metal interface per overall layer thickness, and $1/\Phi$ is the consumed metal thickness per product layer thickness.

Assuming hypothetically that the strain in the product layer is elastic in nature, the force per width would be given by

$$F_w = -\frac{Y_s\Delta V_{m/f}}{3(1-v_s)} \tag{5}$$

Combining Eqs. (10) and (11), the elastic stress generated is

$$F_w = \frac{\Omega_p Y_s q}{6F(1-v_s)}\left(\frac{1}{\Phi} - t_A\right) \tag{6}$$

While t_A in the product layer is unknown, passive films on iron and steel generally support both cation and anion transport by migration through grain boundaries between nanocrystals [42], and the presence of the outer precipitated product layer indicates that t_A must be less than unity. For an example calculation, t_A is taken to be 0.5, with Ω_p and Φ assigned values of 26.4 cm³/mol and 3.7 for Fe(OH)$_2$. For the maximum charge density of 300 mC/cm² in Fig. 5.9 (b), the calculated force is close to -10⁴ N/m, two orders of magnitude higher than the measured value. Therefore, despite the uncertain transport number, it is likely that the volume expansion due to oxide formation is accommodated by plastic rather than elastic deformation. The yield stress of the compact corrosion product was estimated to be 330 MPa from nanoindentation hardness measurements [30]. At the force levels in Fig. 5.9 (a), the compact product layer thickness would be F_w/σ_Y or 100 to 200 nm where σ_Y is the yield stress. This range is compatible with the submicron layer thickness of the

compact layer revealed by nanoindentation [30]. Thus, the calculation supports the view that the porous precipitated layer is stress-free.

If the stress in the product layer remains close to the yield stress, the force can be approximated as $F_w \cong \sigma_Y h_p (A_p/A_s)$. Here σ_Y and h_p are the yield stress and thickness of the compact portion of the product layer, A_p is the area covered by the product layer (i. e. the entire oxidized surface area along grain boundaries) and A_s is the projected steel surface area. Assuming that the compact layer thickness remains constant, the increase of compressive force over time is due to increase of A_p as intergranular corrosion spreads over the surface and penetrates into the metal. Thus, the stress measurement is seen to be a sensitive indicator of internal oxidation during intergranular corrosion, arising specifically from the compact product layer and not from the precipitated porous oxide seen in SEM. Indeed, the force transient at -0.575 V suggests oxidation at times less than 10 min, which is not apparent in cross-sectional SEM images at later times. Note that Fig. 5.9 (a) reveals different time dependence of force and current density at the two higher potentials: while force increases steadily, current density reaches a maximum and then decays. The different trends arise because current density depends on both corroding area and the corrosion product thickness, increasing at first as IGC spreads and decreasing at longer times due to growth of the outer product film.

5.5. Relevance to mechanisms of intergranular corrosion and stress corrosion cracking
         The present morphological observations reveal that at potentials of -0.521 and -0.478 V in the range of high SCC susceptibility, intergranular corrosion is centered at triple junctions and penetrates into lateral grain boundaries surrounding the triple junction. High-angle cross section images at -0.521 V show that corrosion at triple junctions takes the form of triangular wedges or notches, as illustrated in Fig. 5.5. At a potential near the active dissolution peak, the images reveal no precipitated internal dissolution product, and corrosion proceeds by selective grain etching. The shallow wedge shape near the passivation potential is explained by a constant dissolution velocity V_s on the grain surface and a slightly higher velocity V_{gb} at the grain boundary itself (Eq. (3)). Stress measurements provide evidence for a compact surface layer at the two higher potentials, which likely regulates V_s. The mechanism explaining the higher dissolution rate on the boundary is less evident. Open crevices are found along corroding grain boundaries at -0.521 V and -0.478 V (Fig. 5.5), and the absence of a porous product would reduce the resistance for mass transport along the boundary. Others have proposed that grain boundary segregated carbon is important for intergranular SCC of low-carbon steels [38, 43]. However, SEM images of shallow angle-polished specimens reveal no evidence for segregated phases at the boundaries. Wedging stresses due to the compact corrosion product layer at the grain boundary could assist corrosion propagation along the boundary [25].

The IGC morphology evolution described here may be related to the strong correspondence between the potential and pH ranges for SCC and IGC [15, 44]. Wendler-Kalsch suggested that wedges produced by corrosion at grain boundaries may induce sufficient stress concentrations to initiate stress corrosion cracks [13]. Indeed, a critical finding of both Ref. [13] and the present work is that wedge or notch features are found only in the potential range where steel is vulnerable to SCC. However, it is not clear that the relatively blunt wedges in Fig. 5.2 can generate significant stress concentration to influence SCC. It is possible that notches with smaller angles and hence

larger stress concentrations may be produced at longer exposure times, or by synergistic enhancement of intergranular corrosion by external stress [15]. Another possible reason for the importance of grain boundary oxidation in SCC is suggested by the EDS measurements in Fig. 5.6 which revealed selective oxidation of Si solute atoms. Preferential oxidation of reactive solutes may produce non-equilibrium metal vacancies, and vacancy-dislocation interaction can explain the reduced local hardness near corroded grain boundaries recently detected by nanoindentation [30, 45]. Since vacancies associated with grain boundary oxidation would be present only at potentials or high cracking susceptibility, the possible involvement of vacancies in the SCC mechanism should be considered. A third possible role of grain boundary oxidation in SCC is that wedging stresses due to the compact corrosion product layer at the grain boundary could directly assist grain boundary fracture [25].

5.6 Modeling framework for morphology evolution during corrosion experiment

A mechanistic COMSOL Multiphysics model is developed to enable obtaining important insights in the process. We performed model guided corrosion experiments to further validate the modeling results. Fig. 5.10 shows the schematic of the vacancy diffusion model, where a preferential oxidation of silicon atoms on the steel surface causes the generation of non-equilibrium vacancies. The mechanism is based our experimental findings of, 1) Nano-indentation measurements showing the presence of a layer of reduced hardness near corroded grain boundaries which suggests the presence of nonequilibrium vacancies and 2) EDS measurements revealing an elevated Si concentration in the corrosion product. The vacancies generated at the surface, due to the oxidizing silicon atoms, move towards grain boundaries under the influence of vacancy concentration gradient. The grain boundaries provide a fast diffusion pathway for Fe atoms, which diffuse towards the incoming vacancies, thereby causing the vacancies to accumulate near the top of the grain boundary. This fast diffusion process effectively makes the vacancy concentration zero at the grain boundaries. The recession caused due the accumulating vacancies at the top of the grain boundaries is given by grain boundary dissolution velocity V_{gb}, while the adjacent surface dissolution velocity is denoted as V_s. The ratio of these two velocities is related to the grain boundary wedge angle α as given by Eq (3).
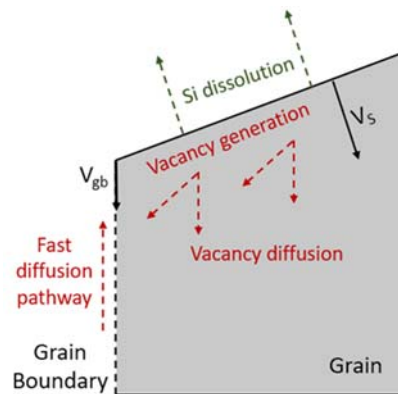
Fig. 5.10: Diffusion model for vacancies introduced by selective Si oxidation. Vacancy diffusion along grain boundaries enhances V_{gb} Vgb relative to V_s, accounting for the triangular wedge shape.
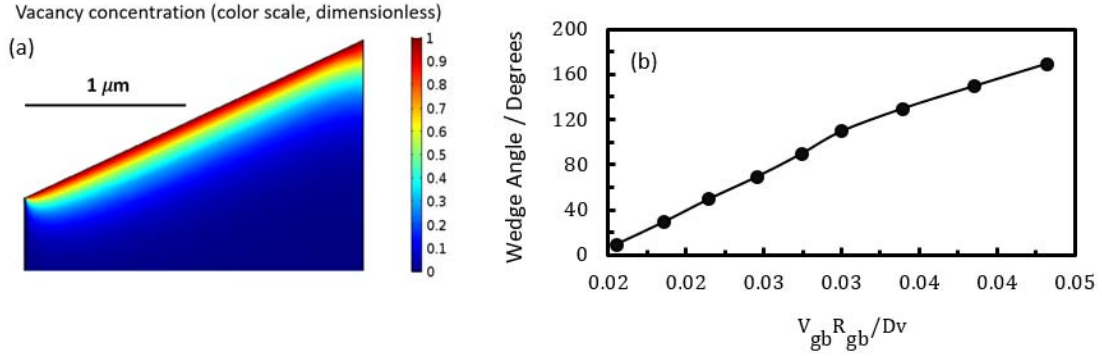
Fig. 5.11: Results from implementation of the vacancy diffusion mechanism in finite element simulation (a) COMSOL simulation domain for a wedge angle of 130° (b) Wedge angle as a function of Peclet number, $Pe = V_{gb}R_{gb}/D_V$.

Figure 5.11 shows the results obtained from the implementation of the vacancy diffusion model in a finite element solver COMSOL Multiphysics. Fig. 5.11 (a) shows the simulation domain for a wedge angle $\alpha = 130°$. The model was run for different values of the wedge angle ranging from to $\alpha = 170°$. For all values of the wedge angle, the diffusion boundary layer is found to be uniform across the inclined surface and of the order of ~ 100 nm. Fig. 5.11 (b) shows the variation of the wedge angle as a function of Peclet number, defined as $Pe = V_{gb}R_{gb}/D_V$. Since Peclet number is

directly proportional to the corrosion rate or the current density, the result shown in Fig. 5.11 (b) implies that for a low corrosion rate, sharper narrow-angle wedges are formed and vice-versa.
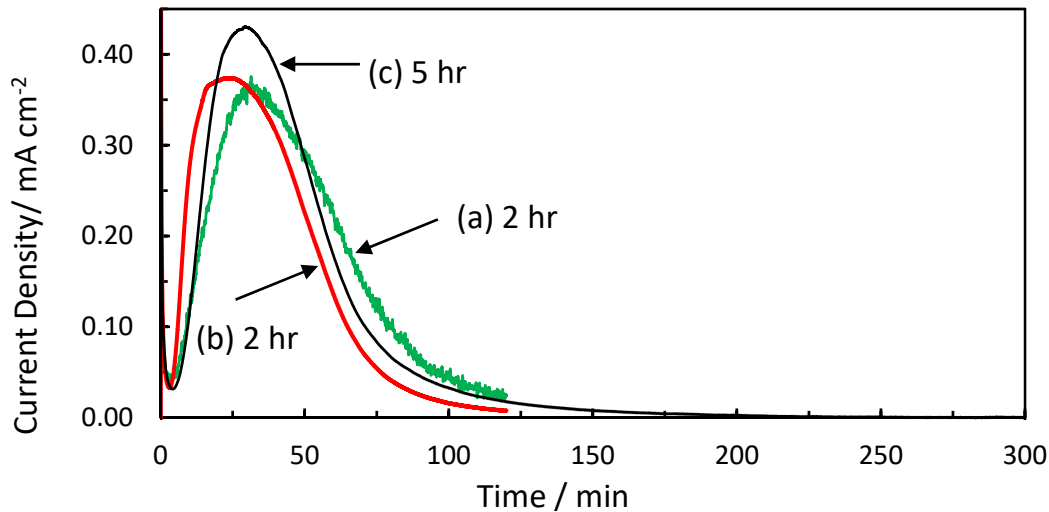
Fig. 5.12: Current transients for constant potential experiments performed at 0.521 V vs Ag/AgCl in 1 M NaHCO$_3$ solution (a) and (b) 2 hr experiments (c) 5 hr experiment.

The vacancy diffusion model is extended to include a transient wedge morphology evolution. We compare the model predicted grain boundary (GB) wedge apex angles with the experimental values. Fig. 5.12 shows the current density transients for constant potential experiments at -0.521 V for 2 hr and a 5 hr corrosion experiment and Fig. 5.13 shows the corresponding cross-sectional

micrographs. The current density transients differ between the two 2 hr experiments in Fig. 5.12 (a) and (b), such that the minimum current for Fig. 5.12 (b) is 2 orders of magnitude lower than the peak current compared to an order of magnitude current density change for the Fig. 5.12(a) experiment. Further, the minimum current density is three orders of magnitude lower than the peak current density for the 5 hr experiment (Fig. 5.12 (c)). The average apex angle determined from the cross-sectional SEM micrographs, as shown in Fig. 5.13, are 136°, 74.2° and 27.1° corresponding to the experiments in Fig. 5.12 (a), (b) and (c) respectively. It is apparent that the average wedge apex angle decreases with decreasing current density and vice versa. The extended periods of lower current densities in the 2 hr (Fig. 5.12 (b)) and the 5 hr (Fig. 5.12 (c)) experiments lead to the formation of wedges with smaller apex angles compared to the 2 hr experiment in Fig. 5.12 (a).
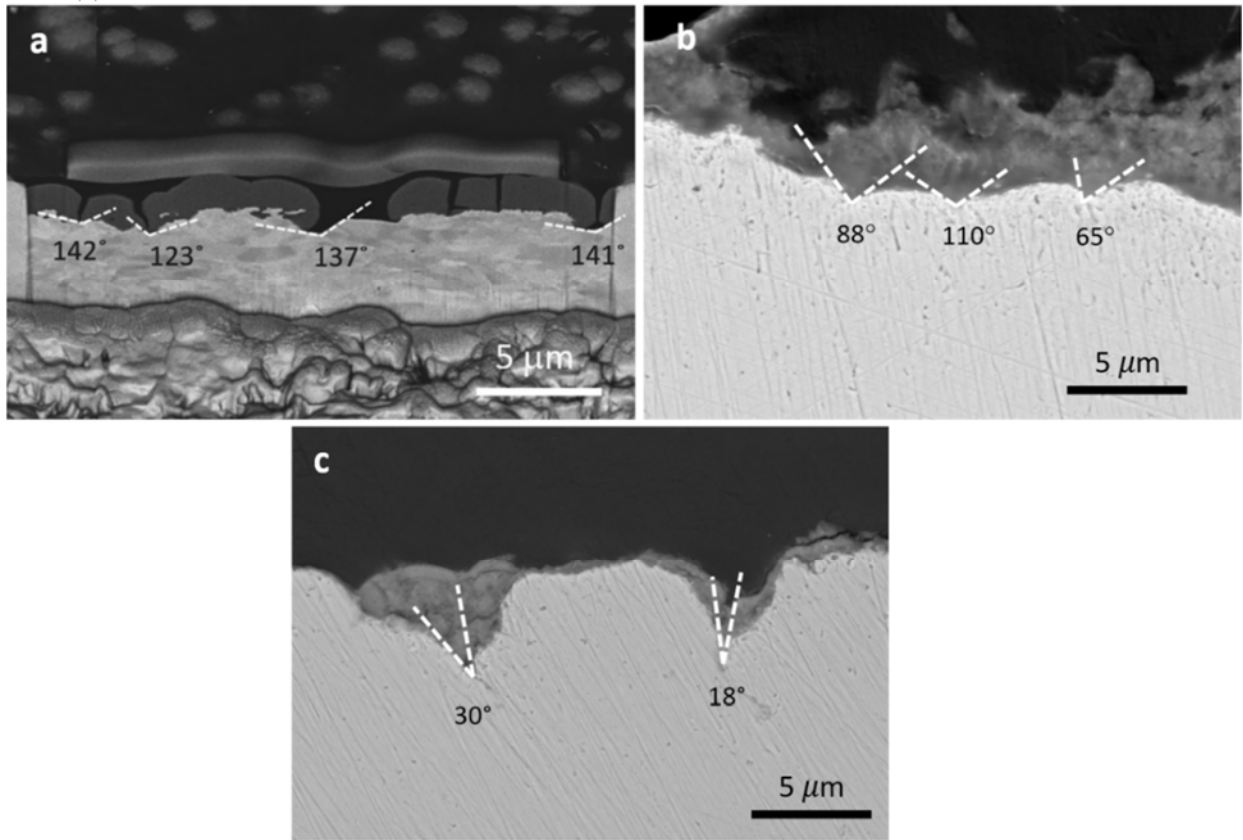
Fig. 5.13: SEM cross-sectional micrographs depicting GB wedges. (a), (b) and (c) Respectively correspond to the experiments shown Fig. 5.12 (a), (b) and (c).

For a quantitative comparison of the variation in the apex angles between the experiments, finite element simulations were run for the current densities in Fig. 5.12. Figure 5.14 shows the results of the time-dependent finite element study for the 5-hour corrosion experiment. The color scheme represents the dimensionless concentration of vacancies, where the color scale is given on the right. The starting geometry at $t = 0$ is the rectangular domain represented by the black outline. For short durations of $t = 1$ hr and $t = 2$ hr, shown in Fig. 5.14 (a) and (b), respectively, the wedges formed have approximately constant wedge angles. For $t < 2$ hr, the change in the current density is relatively small (Fig. 5.12 (a)), implying that the dissolution velocities V_S and V_{gb} remain relatively

unchanged. From Eqs. (1) and (2), for constant dissolution velocities, the wedge angle also becomes constant. The result is consistent with the observation of constant wedge angles for short duration corrosion experiments.
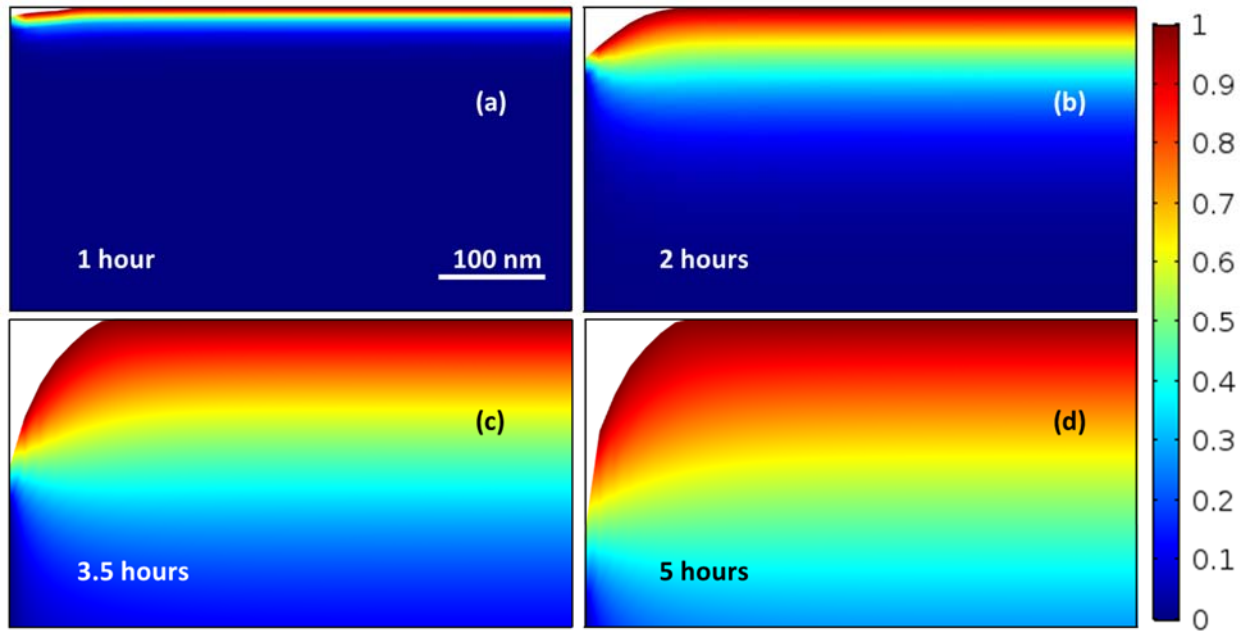
Fig. 5.14: Wedge morphology evolution obtained from the time-dependent finite element study of the vacancy diffusion model in COMSOL at different times of (a) 1 hour (b) 2 hours (c) 3.5 hours (d) 5 hours.

For longer durations of $t > 2\,\mathrm{hr}$, a varying slope is observed along the dissolving surface. As evident from Fig. 5.14 (c) and (d), surface slope close to the GB become progressively steeper, while the slopes away from the GB are shallower. As the current density decays with increasing time (Fig. 5.12 (a)), the surface dissolution velocity V_s also decreases considerably. Since wedge angle varies inversely with the surface dissolution velocity, the instantaneous wedge angle near the GB becomes narrower with the current decay. The effect of a sharp wedge angle at the GB on the wedge surface near the GB is determined by the relation in Eq. 3, with the surface closer to GB affected more compared to the surface father from the GB. The simulation wedge profile at 5 hours (Fig. 5.14 (d)) is qualitatively consistent with the experimental wedge profiles for the 5-hour corrosion experiment depicted in Fig. 5.12 (b).

The apex angles obtained from the simulations were measured and plotted at different time durations during the process in Fig. 5.14. It was revealed that there is an overall decrease in the wedge apex angle as the current density decreases over time, consistent with our previous result relating the wedge apex angle with the current density. The final wedge apex angles obtained from the simulations were able to accurately predict the experimental values for all the experiments, as shown in Fig. 5.15. The encouraging consistency between the experimental and modeling results for the time-dependent case further validates the vacancy-diffusion controlled enhancement of GB corrosion model.
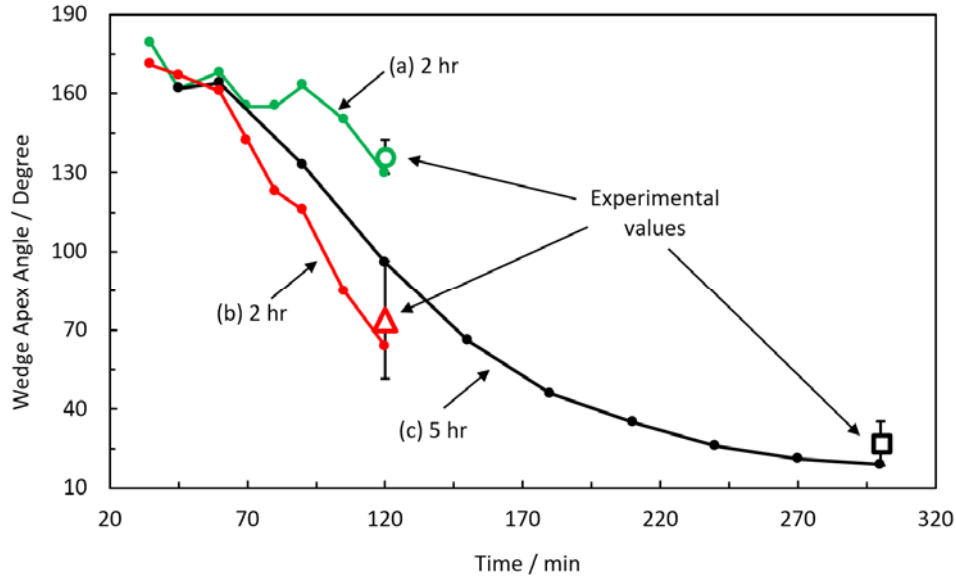
Fig. 5.15: (a), (b) and (c) GB wedge apex angles variations over time obtained using time-dependent finite-element simulations using current densities shown in Fig. 1 (a), (b) and (c) respectively. Data points (a), (b) and (c) present the experimental values obtained from SEM micrographs (Fig. 2) for the corresponding corrosion experiments. Error bars present the standard deviations of the experimental wedge apex angles.

6. Results of Nanoindentation study of Corrosion-Induced Grain Boundary Degradation in a Pipeline Steel

6.1 Experimental and theoretical methods

6.1.1 *Nanoindentation experiment*

Samples of a high strength low carbon steel (API 5L X70) were used in corrosion experiments. The primary alloying elements were Mn (1.70 wt%), Si (0.37 wt%), Cr (0.06 wt%) and C (0.09 wt%). The majority ferrite phase consisted of nearly equiaxed grains with about 5 μm average grain diameter, while the minority pearlite phase was composed of elongated grains less than 5 μm in width. The steel specimens were polished to 800 grit finish, cleaned and mounted in an electrochemical cell with an Ag/AgCl reference electrode and Pt counter electrode (cited potentials are with respect to Ag/AgCl). The test solution was 1 M $NaHCO_3$ at pH 8.1 at room temperature. A potential of -1.0 V was applied for 5 min to cathodically reduce surface oxide, and then the potential was stepped to a value of -0.521 V within the active dissolution region of the current-potential curve, and held at this level for 2 h. The corroded steel samples were polished at shallow angles relative to the original surface to reveal cross sections through the intergranular corrosion layer, followed by nanoindentation testing around grain boundaries. The polishing angle was estimated as 0.06° by measurement of the apparent corrosion product layer thickness [47]. Nanoindentation tests used a Hysitron TI 950 TriboIndenter with a 90° cube corner diamond indenter tip. Multiple lines of shallow indents were imposed perpendicular to a GB and 1 μm apart. Within each line, indents with 250 μN peak load were spaced at 0.5 μm intervals to avoid overlap

of the indentation process zones [48, 49]. A height topological scan is generated by the indenter tip and shown in Fig. 6.2(a). Further experimental details are available elsewhere [46, 47].

6.1.2. Molecular dynamics simulations

Molecular dynamics calculations to simulate the indentation experiments were performed on a domain representing an iron bcc single crystal. The computational cell with dimensions 150 x 150 x 75 Å enclosed 143,312 atoms. The atomistic simulator LAMMPS was employed for MD calculations [50]. Two interatomic potentials based on the embedded atom method were utilized for iron-iron and iron-hydrogen interactions [51, 52]. The results were analyzed using the dislocation analysis tool in OVITO [53]. Different vacancy concentrations in the range 0-1 at.% were realized by random deletion of Fe atoms from the perfect lattice. Interstitial H atoms were randomly introduced into the lattice at selected interstitial sites [54, 55]. Prior to indentation, the atomistic models were relaxed at a constant temperature of 1 K for 50 ps, under the canonical ensemble (constant volume and temperature). The low temperature was imposed to ensure immobility of the introduced vacancies. Periodic boundary conditions were used along the <100> and <010> directions, while non-periodic and shrink-wrapped boundary conditions were used in <001> direction. The atoms within the bottom layer of the model with thickness 10 Å were rigidly fixed. For each vacancy or hydrogen concentration, six different initial configurations were generated and analyzed to characterize the statistical variation of the simulation results.

Nanoindentation simulations were performed using a rigid spherical indenter with radius $R = 50$ Å up to an indentation depth of 20 Å, under the micro-canonical ensemble (constant volume and energy). Although the temperature was initially set to 1 K, a very small temperature fluctuation with a peak of 3 K was recorded during the indentation loading stage. The indentation axis was chosen to be along the <001> direction. The initial position of the indenter was located at the center of the simulation cell. The indenter applied a force on each atom in the material sample with magnitude

$$F(r) = \begin{cases} -K(r-R)^2, & r < R \\ 0, & r \geq R \end{cases}$$

(8)

where R is the indenter radius, r is the distance between the indenter center and the atom, and the constant K is 10 eV/Å^2. The indenter speed of 5 m/s was applied with a time step of 2 fs. It should be noted that the indentation speed of the simulations is relatively high compared to the experiments, though it is sufficiently low to maintain the equilibrium state in the simulations and qualitatively achieve the targeted results.

6.2. Results and discussion of GB degradation

6.2.1 *Nanoindentation experimental results*

The SEM micrograph in Fig. 6.1(a) illustrates the morphology of the subsurface intergranular corrosion layer revealed by shallow-angle polishing. The light gray-shaded regions are the roughly equiaxed ferrite grains. IGC attack produced crevices at triple junctions shown as black-shaded areas surrounded by approximately 1 μm thick dark gray-shaded oxide-carbonate corrosion product layers [46]. Figure 6.1(b-d) depicts EDS intensity maps for Fe, O, and Si contents, respectively. The GB corrosion product layer is mainly composed of Fe and O. Figure 1(e) shows EDS spectra for region 1 within grain interior and region 2 within GB corrosion product layer, as highlighted in Fig. 6.1(a). The EDS spectra shows the presence of Si in the GB corrosion product layer, thus demonstrating oxidation of Si solute atoms at grain boundaries.

Figure 6.2(a) is an atomic force microscope surface topography scan showing a crevice at the GB triple junction, with four lines of NI imprints across the GB at different distances from the triple junction. Lines 2 and 3 are close to the GB crevice, where an approximately 1 μm thick corrosion product should be found based on SEM images as in Fig. 6.1 (a). The corrosion product layer at line 3 should be much thinner than 1 μm, and line 4 is beyond the maximum penetration of corrosion. Figure 6.2(b) shows a set of load-indentation depth curves at the different locations indicated in Fig. 6.2(a). The initial elastic Hertzian contact response of the base material is also marked on Fig. 6.2(a) for indentation modulus ($E = 210$ GPa) and indenter tip radius ($R = 350$ nm) [56]. Within the first few nanometers, all curves exhibited similar responses that follow Hertzian contact behavior. Thereafter the curves corresponding to indents placed closer to the GB (curves C and D) started deviating from the elastic response at shallower depth (2 nm at 20 μN), compared to indents further away from GB and closer to grain interior (curves A and B, 6 nm at 60 μN). These deviation loads (or displacements) can be associated with the critical load required for incipient plasticity [57].

All indentation curves exhibited multiple displacement bursts. Displacement bursts have been linked with several different mechanisms such as dislocation nucleation or propagation [57-59], brittle cracking of the native oxide layer [60], and surface roughness [61]. In the current experiments, special care was taken to ensure that the surface roughness was significantly smaller than the indenter tip radius. The average geometric roughness for each indentation site was measured to be smaller than 5 nm over 200 x 200 nm^2. Therefore, the first displacement burst event on every curve can be safely considered as homogenous dislocation nucleation (HDN), when the critical nucleation stress is reached underneath the indenter tip [57-59]. The critical stress required to nucleate a homogenous dislocation loop $\tau|_{HDN}$ occurs at the maximum shear stress underneath the indentation surface $\tau_{max}|_{burst}$. This stress level can be assessed from the critical load associated with the first displacement burst event, and is given by

$$\tau\Big|_{HDN} \approx \tau_{max}\Big|_{burst} = 0.31\left(\frac{6\,E^2}{\pi^3 R^2}P_{burst}\right)^{1/3}$$

(9)

where P_{burst} is the measured load corresponding to the first displacement burst [57]. Figure 6.2(c) shows the spatial variation of the average of P_{burst} within the two grains along lines 3 and 4 as a function of distance from the GB. Loads were normalized by that of the grain interior. On line 3 (which will be compared with the MD simulation), a 55-60 % drop is detected in P_{burst} near the GB compared to the bulk of the grains. From Eq. (9), this implies an approximately 25% degradation in the barrier stress P_{burst} level for HDN, and therefore an enhanced plasticity with a lower dislocation nucleation barrier. Line 2 (not shown here) exhibited nearly the same spatial modulation as line 3, but with a lateral shift corresponding to the thickness of the GB corrosion product. The observed trend of P_{burst} modulation was found at other triple junctions on the same surface, with a spatial modulation zone 1-2 μm from the GBs. To highlight the significance of the observed reduction in P_{burst} close to corroded GBs, note that line 4, located beyond the corrosion-affected region, exhibits the opposite trend of P_{burst} with increased levels close to the GB. Other sets of NI scans on uncorroded surfaces showed statistical variations of P_{burst} with similar increased levels closer to the GB. Such increases are typically understood in terms of dislocation pile-up at GBs [61].
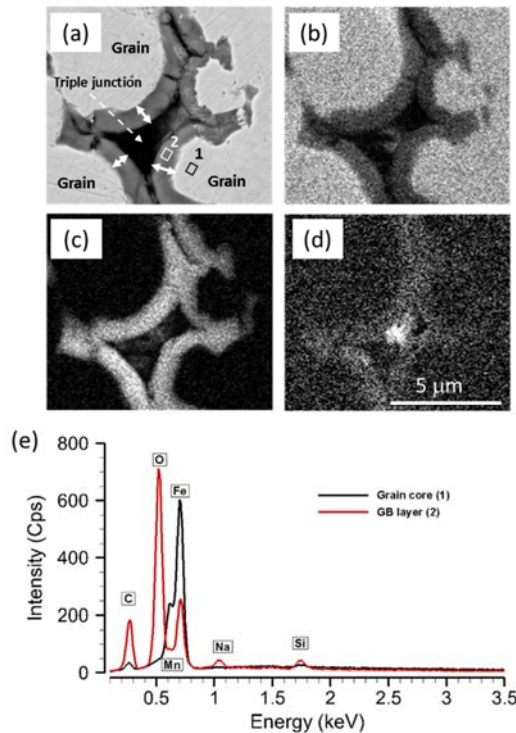

Fig. 6.1. (a) SEM image of the angle-polished corroded surface, showing the IGC attack at a triple junction. (b-d) EDS intensity maps showing Fe, O, and Si content, respectively. (e) EDS spectra within the selected regions 1 and 2.
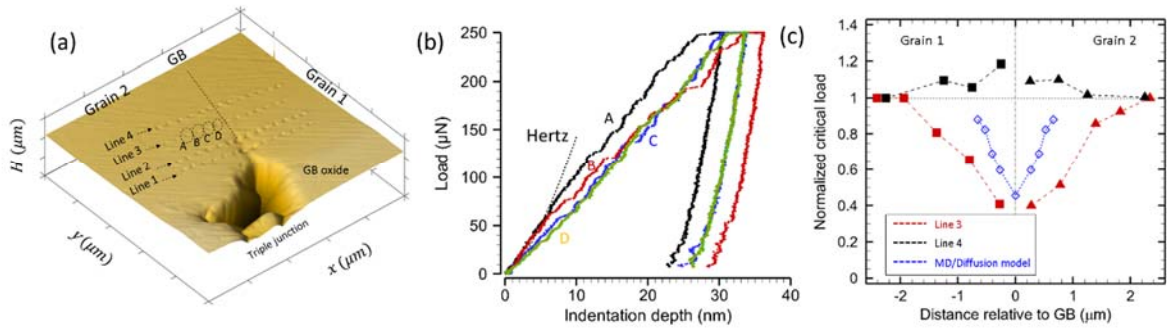
Fig. 6.2. (a) AFM image in surface gradient mode showing the grain boundary and the locations of the imposed lines of nanoimprints. (b) A representative set of force-indentation depth curves for the indents on line 2 at different distances from the GB, along with Hertzian fit for spherical contact, (c) the critical load for the first displacement burst (normalized by the critical loads obtained for the interior of the grains), along with predictions of the MD/vacancy diffusion model (Eq. (10)).

6.2.2 *Molecular dynamics simulation results*

MD simulations using the embedded atom method were employed to explore the roles of hydrogen and vacancy defects in the NI response, and to identify the atomistic mechanisms responsible for corrosion-induced softening near the GB. Nanoindentation on domains representing bcc Fe single crystals was compared to the response of the same domains with various concentrations of either vacancies or hydrogen. Figure 3(a) shows the starting configuration of the atomistic model cell for 1 % (atomic percent) vacancy concentration, with light shading used to highlight atoms neighboring vacancies. Fig. 6.3(b) shows the load-indentation depth curves for three different vacancy concentrations, along with the perfect crystal response. The initial elastic response of the crystal showed a minor gradual softening with increase of the atomic vacancy concentration. All loading curves exhibited load bursts at critical loading levels that tended to decrease with increasing vacancy concentration. Simulations produced load rather than displacement bursts as in Fig. 6.2(b), since the displacement rate was controlled. For perfect crystal, simulation results showed that multiple dislocations nucleated simultaneously, yielding a large load burst. However, with increase of the vacancy concentration, successive and discrete dislocation nucleation events were observed, leading to gradual stair-case bursts as shown in the curve for 0.5 % vacancy concentration. It is worth noting that all the load-indentation depth curves exhibited the same average slope after exhaustion of the load burst events, due to a similar lattice resistance for dislocation mobility. This trend confirms that these dispersed atomic-scale vacancies, differently from nanoscale vacancy clusters which usually act as obstacles to dislocation migration, can reduce the dislocation nucleation barrier, while they may not significantly impact dislocation migration kinetics. Figure 6.3(c) shows the load-indentation depth curves for different

H atomic concentrations, along with the curve for the perfect crystal for comparison. There was an observable softening within the initial elastic part of the curves compared to that for the perfect lattice. However, no distinct change was found relative to the perfect crystal for either the critical load or the amplitude of the load bursts.
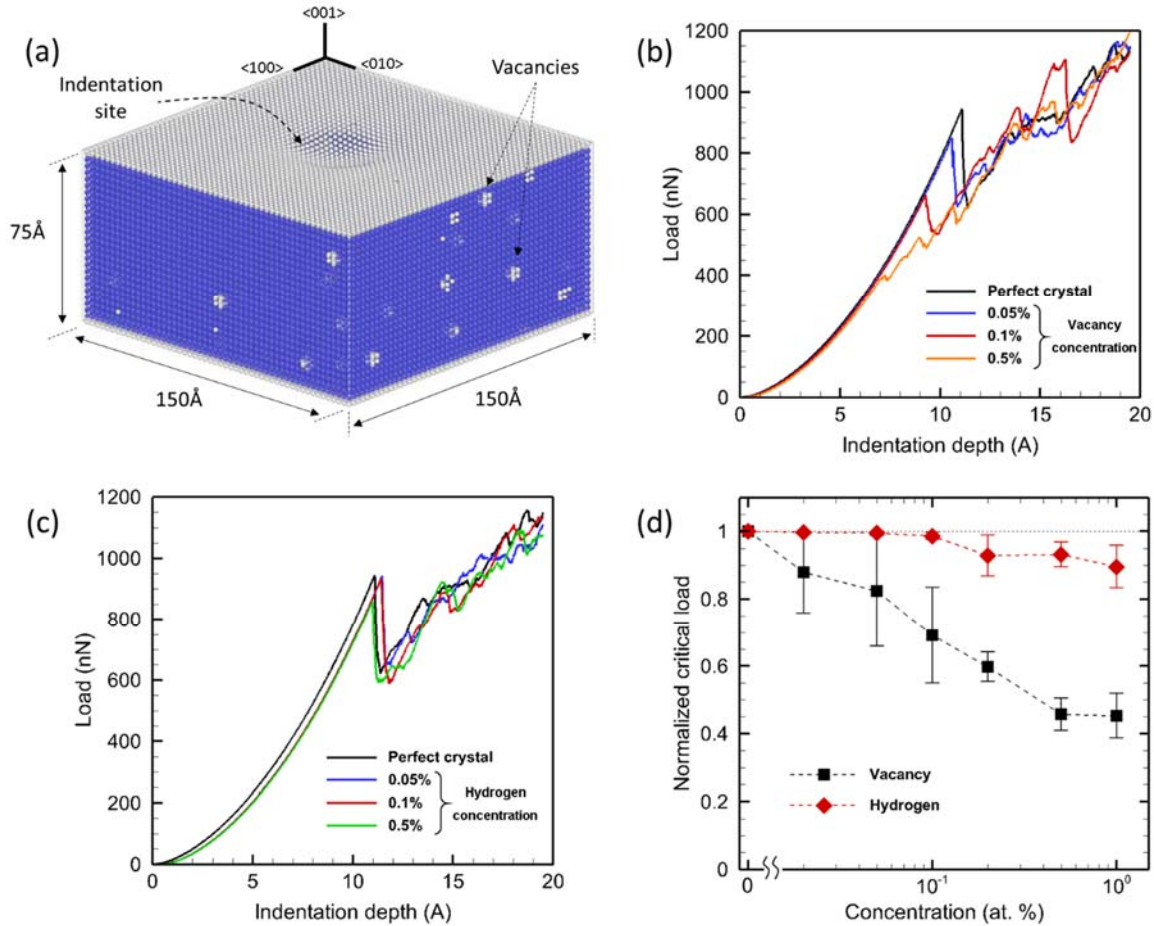
Fig. 6.3. (a) MD simulation model, showing the iron atoms (blue), and the atoms surrounding the lattice vacancies. (b) load-indentation depth curves for different vacancy concentration, (c) load-indentation depth curves for different hydrogen atom concentration. (d) The MD results for the critical dislocation nucleation load (normalized by that of perfect crystal) as a function of the concentration. The error bar is derived from six different geometric rendering of the model.

Figure 6.3(d) summarizes the nucleation load as a function of the concentration of both H and vacancies. Clearly, the presence of vacancies leads to a noticeable reduction of the critical load for the initial load burst. In contrast, interstitial H has an insignificant effect (within 10% for 1 at. % concentration) on the critical load for dislocation nucleation. This trend leads to the conclusion that vacancies rather than interstitial H atoms act as softening agents. Similar simulations were

also performed for a double-sized samples under indentation. The same trend in Fig. 6.3(d) was observed, eliminating the possibility of artifacts due to the limited sample size in the MD model.
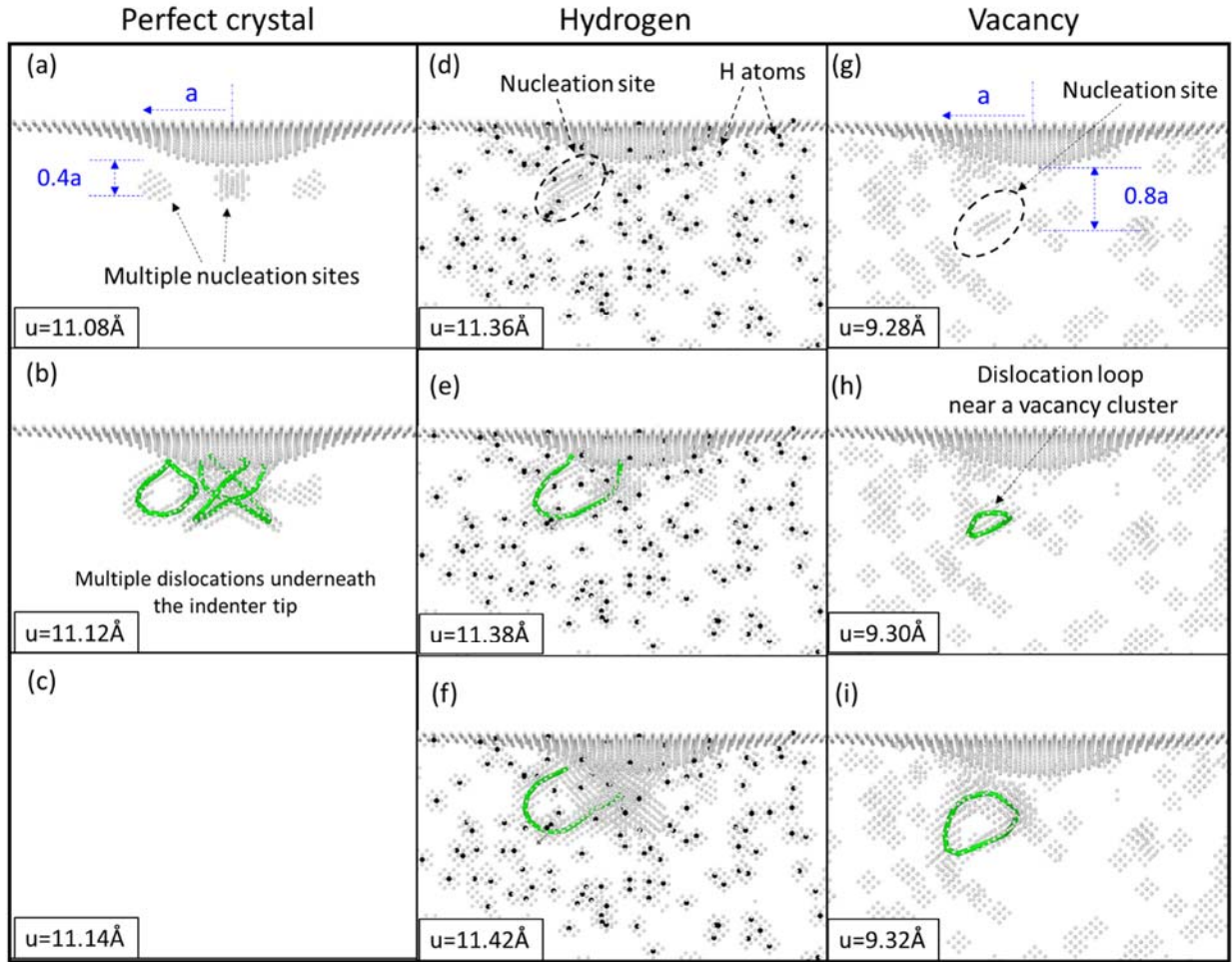
Fig. 6.4: Atomistic simulation results of perfect crystal showing multiple dislocation nucleation and propagation at the critical loading level. Snapshots of atomistic projection with shading of out-of-registry atoms for the perfect crystal (a-c), hydrogen (d-f), and vacancy cases (g-i), highlighting variation of dislocation nucleation characteristics with addition of lattice vacancies and H interstitials.

Figure 4 depicts atomic-scale events during dislocation nucleation and propagation for a perfect crystal in Fig. 6.4(a-c), 0.1% H concentration in Fig. 6.4(d-f), and for 0.1% vacancy concentration in Fig. 6.4(g-i). Each column shows atomistic projections with shading of out-of-registry atoms. Panels (a), (d), and (g) represent the initial Hertzian deformation field, prior to appearance of dislocations; (b), (e), and (h) show the simulation cell immediately after the first dislocation nucleation event, while (c), (f), and (i) represent a later stage showing slight evolution of the nucleated dislocation loops.

For the case of the perfect crystal, Fig. 6.4 (a-c) shows that multiple dislocation loops nucleated under the indenter tip, where the maximum shear stress reached the theoretical strength of the

lattice. In the simulation shown in Fig. 4(a), three nucleation sites were activated by indentation, highlighting the bcc crystal symmetry. The depths of the nucleation sites are approximately 45% of the contact radius a, measured along the indenter line of symmetry from the indenter-crystal interface. The dislocation nucleation site is close to the depth of $0.48a$ for maximum shear stress under spherical contact predicted by Hertzian analysis [56]. Once these dislocation loops nucleated, they migrated under the increasing applied load until intercepting the indenter interface (Fig. 4(b, c)). For 0.1% H concentration, dislocation nucleation exhibits a similar trend as the perfect crystal, except only one of the {110} slip planes was activated. Figure 6.4(d) shows the atomistic configuration immediately before dislocation nucleation, where black-shaded H atoms are surrounded by gray-shaded out-of-registry atoms. Although there are multiple H atoms underneath the indenter tip, a single dislocation nucleated under the indenter, at a depth of $0.52a$ close to that expected for the perfect crystal. The location of the first dislocation nucleation was approximately independent of H atom sites for this particular concentration; however, the existence of H provided preferential nucleation sites for single dislocations, thereby distorting the deformation symmetry. For 0.1% vacancy concentration in Fig. 6.4(g), out-of-registry atom clusters representing atomic relaxations around individual vacancies are present prior to contact with the indenter. Figure 6.4(h) reveals that the first dislocation loop nucleated close to such a vacancy site. The depth of this nucleation site is about 84% of the contact radius a, much larger than $0.48a$ for the perfect crystal case. Thus, the local shear stress at this site would be below that for the first dislocation nucleation in the absence of vacancies (Fig. 6.4(g)). Apparently, the energy barrier for nucleation was reduced at vacancy sites relative to that for the perfect crystal; however, H defects did not lower the barrier significantly. Once nucleated, the dislocation loop grew under the applied load (Figs. 6.4(i)).
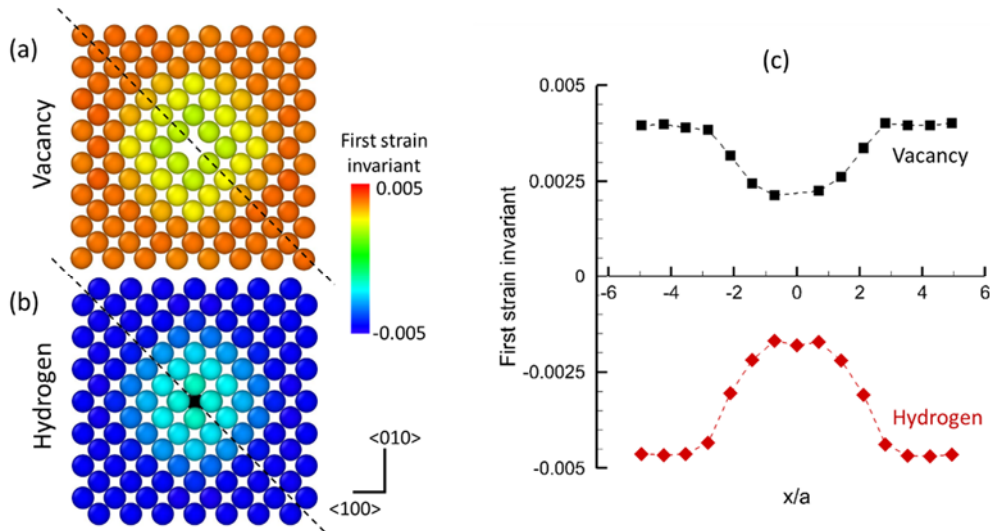

Fig. 6.5: Distribution of first strain invariant on {001} plane, showing initially induced hydrostatic strain by (a) vacancy and (b) hydrogen atom. (c) The line distribution of first strain invariant along <110> direction (dashed lines on (a) and (b)) presented as a function of distance normalized by the atomic distance.

The ability of vacancies but not hydrogen to reduce the energy barrier for dislocation nucleation correlates with the local atomic configuration around defects in the relaxed state before indentation. Figures 6.5(a) and (b) compare the first strain invariant (associated with hydrostatic strain) around a vacancy and H atom on the {001} plane in the relaxed state. Figure 6.5(c) shows the distribution of the first strain invariant along the <110> direction, noted on Fig. 6.5(a, b). In the 0.1% vacancy case, the overall model experiences a tensile (dilation) residual volumetric strain of about 0.40% after relaxation around vacancies. On the other hand, in the 0.1% H case, there is a compressive residual volumetric strain about 0.45% after relaxation around H atoms. MD simulations of the effect of volumetric pre-strain up to 1% on nanoindentation behavior in nickel and palladium single crystals showed that a tensile pre-strain reduced pop-in load, while a compressive lattice strain increased pop-in load [62]. Our results are consistent with these observations, except that the present Fe-H system does not exhibit an increase in the pop-in load even though it shows a compressive residual strain.

6.2.3. *Vacancy diffusion calculation*

Calculations with a vacancy diffusion model were carried out to investigate the origin of corrosion-generated vacancies responsible for softening near GBs. The model hypothesizes that vacancies are injected by oxidation of reactive Si solute atoms at grain boundaries. Accordingly, the vacancy concentration distribution near the GB is calculated and, together with the concentration-dependent critical load from MD, used to predict the spatial variation of critical load for direct comparison to the NI results in Fig. 6.2(c). The evolution of vacancy concentration near the corroding interface is determined by the transient diffusion equation,

$$\frac{\partial C}{\partial t} - v_d \frac{\partial C}{\partial x} = D_v \frac{\partial^2 C}{\partial x^2} \tag{10}$$

where C is the vacancy concentration, v_d is the dissolution velocity of the GB, D_v is the vacancy diffusivity, x is position relative to the corroding interface and time t is measured from the initiation of corrosion at the GB site. A constant interfacial concentration C_{GB} is maintained at $x = 0$, which according to the hypothesis is taken as equivalent to the bulk Si concentration of 0.77 at.%. Since the equilibrium vacancy concentration in steel at ambient temperature is negligible relative to C_{GB}, C is taken as zero far from the interface and at zero time.

Equation (10) was solved numerically using values of 5 x 10^{-17} m^2/s for D_v [63], and 0.013 nm/s for v_d [46]. The vacancy diffusion time is a source of uncertainty in these calculations. As a first approximation, we assume that the diffusion time is the same as the time of corrosion at the applied potential. Based on the location of the GB site probed by NI within the IGC layer [46, 47], corrosion initiated roughly 18 min prior to the end of the 2 h experiment. From the concentration profile at 18 min, values of x were determined at the vacancy concentrations for which MD simulations were carried out (Fig. 6.3(d)). Fig. 6.2(c) compares the resulting theoretical prediction of the normalized critical force vs. distance from the GB to the NI measurements. Remarkably, the normalized load of 0.4 measured close to the GB is nearly the same as that

predicted from the value of C_{GB} derived from the bulk Si concentration. This agreement is evidence for the hypothesis that the vacancies responsible for lattice softening are injected by oxidation of reactive Si atoms. The same mechanism could explain vacancy injection in other alloys that contain solutes with dissolution potentials significantly more negative than the corrosion potential. Fig. 6.2(c) also shows that the predicted thickness of the zone of reduced critical load is about 1 μm, roughly one-half of the experimental thickness. The discrepancy can be attributed to underestimation of the vacancy diffusion distance by the model; diffusion would actually continue on open circuit until vacancies encounter traps such as dislocations and solute atoms.

The present results demonstrate that corrosion-induced vacancy injection occurs in the narrow potential range of active dissolution where steel is highly susceptible to IGSCC. The possible role of vacancies in GB embrittlement during IGSCC should therefore be considered. According to Neeraj et al., aggregation of strain-induced vacancies led to nanovoids that they observed on fracture surfaces of H-embrittled pipeline steels [66]. On the macroscale [64], considering the cohesive behavior of the crack tip, the existence of nanovoids close to GBs might reduce the GB cohesive strength, thereby shielding vacancy-enhanced plastic deformation within the grain boundary and leading to cleavage GB fracture [62, 65].

7. Conclusion and Impact
This work has developed basic understanding of the early stage stress corrosion cracking in high strength pipeline steel through combined experimental and modeling framework. We have quantified the physical and mechanical changes associated with early stage SCC. The experimentally calibrated predictive modeling of the extent of subsurface damage, grain boundary grooving and early stage percolation of shallow cracks to enable further development of NDE corrosion detection techniques. Monitor changes in parameters germane to corrosion prevention, while mitigating the corrosion impact on the pipeline infrastructure.

This work also identified and explained the chemical mechanism of formation of vacancy defects that may participate in grain boundary degradation. It is found that vacancies originate from oxidation of reactive silicon solute atoms at grain boundaries exposed to the electrolyte interface, then diffuse to the corroding grain boundary and facilitate the grooving process. Identification of such mechanism would enable the steel alloy designer to mitigate the susceptibility to SCC through alloying, surface treatments or coatings.

8. Future Work
The completed work under this CAAP agreement highlights many new insight for the detection and monitoring of the early stage of SCC. The main findings that warrants further investigation and analysis are;
- The evolution of vacancies and reduction GB strength have the potential to provide new basis for detection of early stage subsurface damage percolation through ultrasound or eddy current techniques. Two complementary methodologies that should be further

investigated and developed for prospective utilization for in-line assessments.

- The identification of the grain boundary grooving mechanisms will provide pathways for different strategies to counter these chemical threats and mitigate the alloy susceptibility.

- The identified chemical mechanisms is quite sensitive the current material state, as defined by the level of lattice defects (voids and dislocations). These lattice defects are greatly affected by local stress risers. Thus forming a critical compounding and interactive threats between local corrosion and localized stressed (arising from external dents or gauges that may drive local stress levels to surpass the yield strength of the material. This scenario would result in accelerated localized fatigue failure of the pipeline.

9. References Cited

1. B. Lydell, The probability of pipe failure on the basis of operating experience, Vol. 7. American Society of Mechanical Engineers, New York, (2007).

2. G.H. Koch, M.P.H. Brongers, N.G. Thompson, Y.P. Virmani, and J.H. Payer, Corrosion cost and preventive strategies in the United States: report by CC Technologies Laboratories, Inc. Federal Highway Administration, (2001).

3. J.S. McCloy, et al. Materials degradation and detection (MD2): Deep Dive Final Report PNNL 22309. (Pacific Northwest National Laboratory, Richland, WA; 2013).

4. R.W. Staehle, Critical analysis of "tight cracks". Corros. Rev. 28, 1-103 (2010).

5. Anon, Pacific Gas and Electric Company Natural Gas Transmission Pipeline Rupture and Fire San Bruno, California September 9, 2010. Washington D.C.: National Transporation Safety Board, August 30, (2011).

6. J.E. Marr, S.B. Hardy, E. Huuskonen, SCC Integrity Management—Liquid and Gas Pipeline Systems, Marr Associates, Calgary, May2003.

7. P.J. Kentish, Gas pipeline failures: Australian experience. Br. Corros. J. 20 (1985) 139–146.

8. R. N. Parkins, Mechanistic Aspect of intergranular stress corrosion cracking of high pressure gas pipeline. in Corrosion 2000, Paper 00363 (2000).

9. K. Sieradzki, and R. C. Newman, Brittle behavior of ductile metals during stress-corrosion cracking. Phil. Mag. A, 51, 95 (1985).

10. D.A. Jones, A unified mechanism of stress corrosion and corrosion fatigue cracking. Metall. Trans. A, 16, 1133 (1985).

11. T. Magnin, A. Chambreuil, and B. Bayle, The corrosion-enhanced plasticity model for stress corrosion cracking in ductile FCC alloys. Acta Mater., 44, 1457 (1996).

12. R.D. Armstrong, A.C. Coates, Correlation between Electrochemical Parameters and Stress Corrosion Cracking, Corros. Sci., 16 (1976) 423-433.

13. E. Wendler-Kalsch, The effects of film formation and mechanical factors on the initiation of stress corrosion cracking of unalloyed steels in carbonate solutions, Werkst. Korros., 31 (1980) 531-542.

14. R.N. Parkins, S. Zhou, The stress corrosion cracking of C-Mn steel in CO_2-HCO_3--CO_3^{2-} solutions .I. Stress corrosion data, Corros. Sci., 39 (1997) 159-173.

15. R.N. Parkins, S. Zhou, The stress corrosion cracking of C-Mn Steel in CO2-HCO3--CO32- solutions. II. Electrochemical and other data, Corros. Sci., 39 (1997) 175-191.

16. R.C. Newman, Stress-Corrosion Cracking Mechanisms, in: P. Marcus (Ed.) Corrosion Mechanisms in Theory and Practice, CRC Press, Boca Raton, 2011, pp. 499-544.

17. R.D. Armstrong, A.C. Coates, Passivation of Iron in Carbonate-Bicarbonate Solutions, J. Electroanal. Chem., 50 (1974) 303-313.

18. D.H. Davies, G.T. Burstein, The Effects of Bicarbonate on the Corrosion and Passivation of Iron, Corrosion, 36 (1980) 416-422.

19. C.R. Valentini, C.A. Moina, J.R. Vilche, A.J. Arvia, The Electrochemical Behavior of Iron in Stagnant and Stirred Potassium Carbonate-Bicarbonate Solutions in the 0-75oC Temperature Range, Corros. Sci., 25 (1985) 985-997.

20. E.B. Castro, C.R. Valentini, C.A. Moina, J.R. Vilche, A.J. Arvia, The Influence of Ionic Composition on the Electrodissolution and Passivation of Iron Electrodes in Potassium Carbonate Bicarbonate Solutions in the 8.4-10.5 Ph Range at 25-Degrees-C, Corros. Sci., 26 (1986) 781-793.

21. A.M. Riley, J.M. Sykes, The Active Passive Transition in Low-Alloy Steels in Carbonate Solutions, Electrochim. Acta, 35 (1990) 35-45.

22. E.B. Castro, J.R. Vilche, A.J. Arvia, Iron Dissolution and Passivation in K2CO3-KHCO3Solutions - Rotating-Ring-Disk Electrode and XPS Studies, Corros. Sci., 32 (1991) 37-50.

23. J.M. Blengino, M. Keddam, J.P. Labbe, L. Robbiola, Physicochemical Characterization of Corrosion Layers Formed on Iron in a Sodium Carbonate-Bicarbonate Containing Environment, Corros. Sci., 37 (1995) 621-643.

24. B. Gwinner, M. Auroy, F. Balbaud-Celerier, P. Fauvet, N. Larabi-Gruet, P. Laghoutaris, R. Robin, Towards a reliable determination of the intergranular corrosion rate of austenitic stainless steel in oxidizing media, Corros. Sci., 107 (2016) 60-75.

25. D. McNaughtan, M. Worsfold, M.J. Robinson, Corrosion product force measurements in the study of exfoliation and stress corrosion cracking in high strength aluminium alloys, Corros. Sci., 45 (2003) 2377-2389.

26. T. Zhang, W.Y. Chu, K.W. Gao, L.J. Qiao, Study of correlation between hydrogen-induced stress and hydrogen embrittlement, Mater. Sci. Eng., A, 347 (2003) 291-299.

27. H.E. Evans, H.Y. Li, P. Bowen, A mechanism for stress-aided grain boundary oxidation ahead of cracks, Scripta Mater., 69 (2013) 179-182.

28. Ö.Ö. Çapraz, S. Ide, P. Shrotriya, K.R. Hebert, Tensile stress and plastic deformation in aluminum induced by aqueous corrosion, Acta Mater., 115 (2016) 434-441.

29. D. Yavas, P. Mishra, A.F. Bastawros, K.R. Hebert, P. Shrotriya, Characterization of Sub-surface Damage During the Early Stage of Stress Corrosion Cracking by Nano Indentation, C Proc Soc Exp Mech, (2017) 37-44.

30. D. Yavas, P. Mishra, A. Alshehri, P. Shrotriya, K.R. Hebert, A.F. Bastawros, Nanoindentation study of corrosion-induced grain boundary degradation in a pipeline steel, Electrochem. Commun., 88 (2018) 88-92.

31. J. Wang, P. Shrotriya, K.S. Kim, Surface residual stress measurement using curvature interferometry, Exp Mech, 46 (2006) 39-46.

32. Ö.Ö. Çapraz, K.R. Hebert, P. Shrotriya, In Situ Stress Measurement During Aluminum Anodizing Using Phase-Shifting Curvature Interferometry, J. Electrochem. Soc., 160 (2013) D501-D506.

33. G.E. Fougere, L. Riester, M. Ferber, J.R. Weertman, R.W. Siegel, Young's modulus of nanocrystalline Fe measured by nanoindentation, Mater. Sci. Eng., A, 204 (1995) 1-6.

34. L. Beaunier, M. Froment, C. Vignaud, A Kinetical Model for the Electrochemical Grooving of Grain Boundaries, Electrochim. Acta, 25 (1980) 1239-1246.

35. O.V. Kasparova, Peculiarities of intergranular corrosion of silicon-containing austenitic stainless steels, Prot. Met, 40 (2004) 425-431.

36. J.Q. Wang, A. Atrens, D.R. Cousens, P.M. Kelly, C. Nockolds, S. Bulcock, Measurement of grain boundary composition for X52 pipeline steel, Acta Mater., 46 (1998) 5677-5687.

37. J.Q. Wang, A. Atrens, D.R. Cousens, C. Nockolds, S. Bulcock, Boundary characterization of X65 pipeline steel using analytical electron microscopy, Journal of Materials Science, 34 (1999) 1711-1719.

38. A. Atrens, J.Q. Wang, K. Stiller, H.O. Andren, Atom probe field ion microscope measurements of carbon segregation at an, Corros. Sci., 48 (2006) 79-92.

39. B. Ingham, M. Ko, N. Laycock, J. Burnell, P. Kappen, J.A. Kimpton, D.E. Williams, In situ synchrotron X-ray diffraction study of scale formation during CO_2 corrosion of carbon steel in sodium and magnesium chloride solutions, Corros. Sci., 56 (2012) 96-104.

40. B. Ingham, M. Ko, N. Laycock, N.M. Kirby, D.E. Williams, First stages of siderite crystallisation during CO_2 corrosion of steel evaluated using in situ synchrotron small- and wide-angle X-ray scattering, Faraday Discuss., 180 (2015) 171-190.

41. J.C. Nelson, R.A. Oriani, Stress Generation During Anodic-Oxidation of Titanium and Aluminum, Corros. Sci., 34 (1993) 307-326.

42. P. Marcus, V. Maurice, H.H. Strehblow, Localized corrosion (pitting): A model of passivity breakdown including the role of the oxide layer nanostructure, Corros. Sci., 50 (2008) 2698-2704.

43. L.M. Long, H.H. Uhlig, Effect of Carbon and Oxygen in Iron on Stress Corrosion Cracking in Nitrate Solution, J. Electrochem. Soc., 112 (1965) 964-967.

44. R.N. Parkins, Mechanistic aspects of intergranular stress corrosion cracking of ferritic steels, Corrosion, 52 (1996) 363-374.

45. E.K. Njeim, D.F. Bahr, Atomistic simulations of nanoindentation in the presence of vacancies, Scripta Mater., 62 (2010) 598-601

46. D. Yavas, A. Alshehri, P. Mishra, P. Shrotriya , A.F. Bastawros, K.R. Hebert, Morphology and stress evolution during the initial stages of intergranular corrosion of X70 steel, Electrochim. Acta. 285 (2018) 336-343.

47. D. Yavas, P. Mishra, A. Alshehri, P. Shrotriya, K.R. Hebert, A.F. Bastawros, Nanoindentation study of corrosion-induced grain boundary degradation in a pipeline steel, Electrochem. Commun. 88 (2018) 88-92.

48. C. Yang, C.T. Lo, A.F. Bastawros, B. Narasimhan, Measurements of diffusion thickness at polymer interfaces by nanoindentation: a numerically calibrated experimental approach, J. Mater. Res. 24 (2009) 970–992.

49. B. Taljat, T. Zacharia, G.M. Pharr, Pile-up behavior of spherical indentations in engineering materials, MRS Proc. 522 (1998) 33–38.

50. H. Van Swygenhoven, Grain boundaries and dislocations, Science 296 (2002) 66-67.

51. S. Plimpton, Fast parallel algorithms for short-range molecular dynamics, J. Comput. Phys. 117 (1995) 1-19.

52. M.I. Mendelev, S. Han, D.J. Srolovitz, G.J. Ackland, D.Y. Sun, M. Asta, Development of new interatomic potentials appropriate for crystalline and liquid iron, Philos. Mag. 83 (2003) 3977-3994.

53. A. Ramasubramaniam, M. Itakura, E.A. Carter, Interatomic potentials for hydrogen in α–iron based on density functional theory, Phys. Rev. B 79 (2009) 174101.

54. A. Stukowski, Visualization and analysis of atomistic simulation data with OVITO–the Open Visualization Tool, Model. Simul. Mater. Sci. 18 (2009) 015012.

55. S. Taketomi, R. Matsumoto, N. Miyazaki, Atomistic study of hydrogen distribution and diffusion around a {112}< 111> edge dislocation in alpha iron, Acta Mater. 56 (2008) 3761-3769.

56. K.L. Johnson, Contact Mechanics, Cambridge University Press, Cambridge UK, 1985.

57. W.W. Gerberich, S.K. Venkataraman, H. Huang, S.E. Harvey, D.L. Kohlstedt, The injection of plasticity by millinewton contacts, Acta Metall Mater. 43 (1995) 1569-1576.

58. S. Suresh, T.G. Nieh, B.W. Choi, Nano-indentation of copper thin films on silicon substrates, Scripta Mater. 41 (1999) 951-957.

59. A. Gouldstone, H.J. Koh, K.Y. Zeng, A.E. Giannakopoulos, S. Suresh, Discrete and continuous deformation during nanoindentation of thin films, Acta Mater. 48 (2000) 2277-2295.

60. M. Pang, D.F. Bahr, Thin-film fracture during nanoindentation of a titanium oxide film–titanium system, J. Mater. Res. 16 (2001) 2634-2643.

61. Y. Shibutani, A. Koyama, Surface roughness effects on the displacement bursts observed in nanoindentation, J. Mater. Res. 19 (2004) 183-188.

62. X. Zhou, B. Ouyang, W.A. Curtin, J. Song, Atomistic investigation of the influence of hydrogen on dislocation nucleation during nanoindentation in Ni and Pd, Acta Mater. 116 (2016) 364-369.

63. M.I. Mendelev, Y. Mishin, Molecular dynamics study of self-diffusion in bcc Fe, Phys Rev B 80 (2009) 144111.

64. V. Tvergaard, J.W. Hutchinson, The relation between crack growth resistance and fracture process parameters in elastic–plastic solids, J. Mech. Phys. Solids 40 (1992) 1377–97.

65. D. Yavas, X. Shang, W. Hong, A.F. Bastawros, Utilization of nanoindentation to examine bond line integrity in adhesively bonded composite structures, Int. J. Fracture 204 (2017) 101-112.

66. S.Z. Li, Y.G. Li, Y.C. Lo, T. Neeraj, R. Srinivasan, X.D. Ding, J. Sun, L. Qi, P. Gumbsch, J. Li, The interaction of dislocations and hydrogen-vacancy complexes and its importance for deformation-induced proto nano-voids formation in □-Fe, Int. J. Plasticity 74 (2015) 175-191.